Faculty of Physics and Astronomy

University of Heidelberg

Diploma thesis
in Physics

submitted by
Paul Andreas Walker
born in Heidelberg

February 2007

Measurement of the Branching Fraction
$$B^+ \to \eta(\to \gamma\gamma)\ell^+\nu_\ell$$
with the BABAR Detector

This diploma thesis has been carried out by Paul Andreas Walker at the

Physikalisches Institut Heidelberg
under supervision of
Prof. Dr. Ulrich Uwer

and at the

Stanford Linear Accelerator Center
under supervision of
Prof. Dr. Vera Lüth and Dr. Jochen Dingfelder

Kurzfassung

Diese Analyse beschreibt die Messung des Verzweigungsverhältnisses des charm-losen semileptonischen B Mesonenzerfalls $B^+ \to \eta(\to \gamma\gamma)\ell^+\nu_\ell$. Die B Mesonen werden in e^+e^- Kollisionen bei einer Schwerpunktsenergie von 10.58 GeV erzeugt, was der Masse der $\Upsilon(4S)$ Resonanz entspricht. Der benutzte Datensatz umfasst 225 Millionen B-Mesonpaare, die mit dem *BABAR* Detektor aufgezeichnet wurden und entspricht einer integrierten Luminosität von 215 fb^{-1}. Die vorgestellte Analyse rekonstruiert nur das semileptonisch zerfallende B Meson und verzichtet auf die Rekonstruktion des zweiten B Mesons im Ereignis. Dadurch erhöht sich die Effizienz der Analyse erheblich. Dies ist die erste Messung des Verzweigungsverhältnisses von $B^+ \to \eta\ell^+\nu_\ell$ mit dem *BABAR* Experiment, die diese Methode benutzt. Eine 2-dimensionale Maximum-Likelihood-Anpassung wird benutzt, um das Verzweigungsverhältnis zu bestimmen. Die Anzahl der rekonstruierten Signalereignisse beträgt 98.7 ± 27.1 $B^+ \to \eta(\to \gamma\gamma)\ell^+\nu_\ell$ Kandidaten. Das kann zu einem Verzweigungsverhältnis von $\mathcal{B}(B^+ \to \eta(\to \gamma\gamma)\ell^+\nu) = (1.28 \pm 0.35_{\mathrm{stat}} \pm 0.29_{\mathrm{syst}}) \cdot 10^{-5}$ umgerechnet werden. Mit diesem Ergebnis und dem Verzweigungsverhältnis von $\eta \to \gamma\gamma$ kann man das Verzweigungsverhältnis von $\mathcal{B}(B^+ \to \eta\ell^+\nu) = (3.25 \pm 0.89_{\mathrm{stat}} \pm 0.74_{\mathrm{syst}} \pm 0.02_{\mathrm{BF}(\eta \to \gamma\gamma)}) \cdot 10^{-5}$ berechnen.

Abstract

This analysis presents a measurement of the branching fraction of the charmless semileptonic B meson decays $B^+ \to \eta(\to \gamma\gamma)\ell^+\nu_\ell$. These B mesons are produced in e^+e^- collisions at a center-of-mass energy of 10.58 GeV, corresponding to the mass of the $\Upsilon(4S)$ resonance. The analysis is based on data recorded with the *BABAR* experiment and corresponds to an integrated on-peak luminosity of 215 fb^{-1} which is equivalent to 225 million $B\bar{B}$ events. The analysis is an untagged analysis that only reconstructs the semileptonic B decay but does not reconstruct the other B meson. This is the first measurement of the branching fraction $B^+ \to \eta\ell^+\nu_\ell$ in the *BABAR* experiment performed with this method. A maximum likelihood fit is used to extract the signal branching fraction. The signal yield is 98.7 ± 27.1 $B^+ \to \eta(\to \gamma\gamma)\ell^+\nu_\ell$ candidates. This results in a branching fraction of $\mathcal{B}(B^+ \to \eta(\to \gamma\gamma)\ell^+\nu) = (1.28 \pm 0.35_{\mathrm{stat}} \pm 0.29_{\mathrm{syst}}) \cdot 10^{-5}$. Using the $\eta \to \gamma\gamma$ branching fraction one can translate this into a branching fraction of $\mathcal{B}(B^+ \to \eta\ell^+\nu) = (3.25 \pm 0.89_{\mathrm{stat}} \pm 0.74_{\mathrm{syst}} \pm 0.02_{\mathrm{BF}(\eta \to \gamma\gamma)}) \cdot 10^{-5}$.

Contents

Chapter 1

Introduction

The *BABAR* experiment at the Stanford Linear Accelerator Center (SLAC) was built to study decays of B mesons. B mesons are bosonic hadrons and consist of two valence quarks, one of which is a b quark. These B mesons are produced in pairs in collisions of electrons and positrons at a center-of-mass energy of 10.58 GeV, i.e. at the $\Upsilon(4S)$ resonance. The main goal of the *BABAR* experiment was to establish CP-violation in the B meson system, which was first observed in 2001. The physics program of the *BABAR* experiment also covers a range of other topics. One field of research are semileptonic B meson decays, in which the b quark in the B meson performs a transition $b \rightarrow c\ell\nu$ or $b \rightarrow u\ell\nu$, where c or u denote the charm and up quarks and represent the hadronic part of the semileptonic decay and ℓ and ν denote leptons and represent the leptonic part of the semileptonic decay. Semileptonic decays are mediated via the weak interaction and allow a study of the weak couplings of quarks. The strengths of the couplings of quarks with different flavors to the W boson are given by the magnitude of the elements of a transformation matrix the so-called Cabibbo-Kobayashi-Maskawa (CKM) matrix. For the above decays, the CKM matrix elements $|V_{cb}|$ and $|V_{ub}|$ are the relevant parameters. $|V_{cb}|$ is known quite precisely (at the 2% level [1]) but $|V_{ub}|$ is only known with a precision of 10-15%. Thus many studies now concentrate on an improvement of the measurement of $|V_{ub}|$.

There are different approaches to measure $|V_{ub}|$, all use that the branching fractions of the $B \rightarrow X_u\ell\nu$ decays are proportional to $|V_{ub}|^2$: the "inclusive" studies measure the total branching fraction of $B \rightarrow X_u\ell\nu$ decays, where X_u denotes a meson which consist of only quarks from the first family. "Exclusive" studies concentrate on a specific X_u meson that is reconstructed. The most precise determinations of $|V_{ub}|$ to this date come from studies of inclusive $B \rightarrow X_u\ell\nu$ decays. The current inclusive world average has an uncertainty of about 7-8% [1]. The dominant contributions to this error are the uncertainties in the momentum distribution of the b quark inside the B meson. In exclusive approaches the dominant uncertainties come from form factor uncertainties needed for the extraction of $|V_{ub}|$. Thus it is important to scrutinize the inclusive results with exclusive measurements since the theoretical uncertainties for the two approaches are complementary.

The *BABAR* experiment has already published results for the exclusively measured decays $B \rightarrow \pi\ell\nu$ and $B \rightarrow \rho\ell\nu$ [2]. To gain a better understanding of charmless semileptonic decays, it is important to also study decays into mesons other than pions and ρ mesons. This is what this thesis does and a branching fraction measurement of the exclusive charmless semileptonic decay $B^+ \rightarrow \eta\ell^+\nu$ is presented. The charged conjugates decay $B^- \rightarrow \eta\ell^-\nu$ is included and always implied.

So far only two measurements of this decay mode exist. A measurement from the CLEO collaboration using 9.7 million $B\bar{B}$ events yielded about 15 signal decays [3]. The second measurement was performed by *BABAR* with a much larger data sample corresponding to an integrated luminosity of 316 fb^{-1}, but resulted in a still quite small signal yield of 45.9 ± 7.1 $B^+ \rightarrow \eta\ell^+\nu$ decays [4].

In the presented untagged analysis, an increase of the signal efficiency by over a factor of ten can be expected. However, since in the present analysis only the $\eta \rightarrow \gamma\gamma$ decay mode is considered and not the full available *BABAR* data set has been used, the expected yield amounts to about 100 $B^+ \rightarrow \eta\ell^+\nu$ decays using an integrated luminosity of 215 fb^{-1}, which should still allow the currently most precise measurement of this decay.

The presented thesis is structured as follows:

- Chapter 2 gives an overview of the theoretical aspects of semileptonic B decays.

- Chapter 3 describes the *BABAR* detector.

- Chapter 4 introduces the data set used in this analysis and gives an overview of the simulated data samples.

- Chapter 5 describes the kinematic properties and the reconstruction of $B^+ \rightarrow \eta\ell^+\nu$ decays.

- Chapter 6 covers the selection of signal candidates and the classification and suppression of background.

- Chapter 7 presents the method used to extract the branching fraction measurement.

- Chapter 8 presents the results of the signal extraction and the branching fraction measurement.

- Chapter 9 gives an overview of the systematic uncertainties.

- Chapter 10 presents a discussion of the results and conclusions.

Chapter 2

Theory

The Standard Model of particle physics (SM) provides a very successful description of the fundamental interaction of matter. It encompasses the electromagnetic force, the strong force and the weak force which are three of the four known fundamental forces. The fourth force, gravitation, is not included in the Standard Model. The decay studied in this analysis, $B^+ \rightarrow \eta \ell^+ \nu$ is mediated by the weak force and contains a $b \rightarrow u$ quark transition. In Figure 2.1 a Feynman graph of the quark transition is shown. The b quark decays weakly into a light quark and an intermediate W boson, which decays into a lepton and a neutrino. The transition of the b quark into the u quark is the hadronic part of the decay, the W boson decay products are the leptonic part of the decay. The coupling strenght involved in the quark transition is described by the CKM matrix element $|V_{ub}|$.

2.1   Semileptonic Decay Kinematics

The transition matrix element for a quark transition can be written as

$$\mathcal{M} = <\Psi_u|H|\Psi_b> = \int \Psi_u H \Psi_b dV \tag{2.1}$$

where Ψ_b and Ψ_u are the initial and final state wave functions of the initial particle (B meson) and the final particle containing a u quark (e.g. π, ρ, or η). H is the Hamiltonian operator which describes the properties of the interaction potential. Integration occurs over the whole volume ($\int dV$).

The connection between the reaction rate (Γ_{ub}) and the transition matrix element V_{ub} is expressed by Fermi's golden rule, which describes the transition on the quark level:

$$\Gamma_{ub} \propto m_b^5 \cdot |V_{ub}|^2. \tag{2.2}$$

The mass of the decaying quark enters in the fifth power.

The CKM matrix element for the $b \rightarrow u$ transition is V_{ub}. V_{ub} is proportional to the
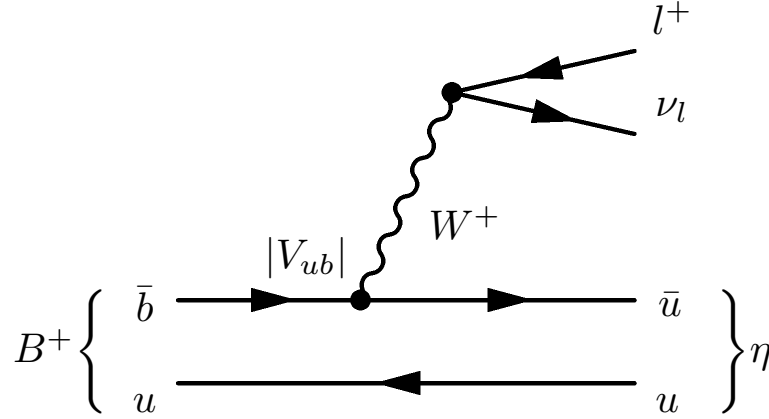
Figure 2.1: Feynman graph of a $b \to u$ quark transition. The b quark decays weakly into a light quark and an intermediate W boson, which decays into a lepton and a neutrino.

expectation value of the transition element:

$$\mathcal{M} = < \Psi_u|H|\Psi_b > = \int \Psi_u H \Psi_b dV \propto G_F \cdot V_{ub} \cdot (L^\mu \cdot H^\mu) \qquad (2.3)$$

where $G_F = g^2/\sqrt{2}M_W^2$ is the Fermi constant and L^μ and H^μ are the lepton and hadronic elements of the weak current. Semileptonic decays are most promising for a measurement of V_{ub}, because as illustrated in Equation 2.3 the hadronic part ($b \to u$ transition) described by the hadronic current H^μ and the leptonic part (lepton and neutrino) described by the leptonic current L^μ are independent of each other. L^μ can be written as

$$L^\mu = u_e \gamma^\mu (1 - \gamma_5) v_\nu \qquad (2.4)$$

where u_e and v_ν are the Dirac spinors of the lepton and neutrino. The H^μ can be written as

$$H^\mu = < \Psi_x|J_{had}^\mu(0)|\Psi_B > \qquad (2.5)$$

where Ψ_B and Ψ_x are the initial and final meson states wave function, and $J_{had}^\mu(0)$ is the Hamilton operator of the weak current. The lepton current can easily be calculated whereas the hadronic current due to low-energy QCD processes is hard to calculate. But because these terms are independent of each other a study of the weak interaction and its quark coupling on the leptonic side without the complication from the hadronic side is possible.

Equation 2.1 and Equation 2.2 describe the transition only correctly if one assumes point-like mesons and neglects the charge distributions and magnetic moment of these mesons. To incorporate the quark distributions inside the meson form factors are introduced. Form factors contain all information about the spatial distribution of the charge and magnetic moment of the particles studied. If form factors were constant factors they would be easy to incorporate but they depend on the four momentum of the W

boson (q^2). The shapes of form factors influence the signal efficiency, which are important for analyses which measure branching fractions of B decays. The normalization of the form factor is important for the extraction of $|V_{ub}|$ (see Section 2.2). Several theoretical calculations for form factors exist: there are Light Cone Sum Rule (LCSR) calculations which are described in Reference [7], [8], and [9], Relativistic Quark Models, such as the ISGW2 model described in Reference [6], and Lattice Quantum Chromo Dynamics (LQCD) calculations which are described in Reference [10].

For this analysis which measures a branching fraction only the q^2 dependence ("shape") of the form factor is relevant: the form factor impacts the shape of the kinematic distributions of the decay. Thus in case any selection requirement on kinematic quantities is used, variations in the form-factor shape can have an effect on the branching fraction measurement. Since the η meson is a pseudo-scalar meson the $B^+ \to \eta \ell^+ \nu$ decay can be described by two form factors: $f_+(q^2)$ and $f_0(q^2)$. The latter form factor can be neglected assuming massless leptons, so that only one form factor needs to taken from theory. For the signal Monte Carlo the most recent results from the LCSR calculation have been used [8].

The contribution of $B \to X_u \ell \nu$ branching fraction to the total semileptonic ($B \to X \ell \nu$) branching fraction is small because it is suppressed with respect to $B \to X_c \ell \nu$ by a factor of $|V_{ub}/V_{cb}|^2$, which is of the order of 10^{-2}:

$$\Gamma(b \to u\ell\nu) \propto \frac{|V_{ub}|^2}{|V_{cb}|^2} \cdot \Gamma(b \to c\ell\nu). \tag{2.6}$$

2.2 Extraction of $|V_{ub}|$

The branching fraction is proportional to the square of $|V_{ub}|$. $|V_{ub}|$ can be extracted from measuring the branching fraction of a $B \to X_u \ell \nu$ decay and with knowledge about the $B \to X_u$ form factor. With $X_u = \eta$ the total decay rate $\Gamma(B \to \eta \ell \nu)$ is given by:

$$\Gamma(B \to \eta\ell\nu) = \int_0^{q^2_{max}} \frac{G_F^2 p_\eta^3}{24\pi^3} \cdot |f_+(q^2)|^2 \cdot |V_{ub}|^2 \cdot dq^2. \tag{2.7}$$

where G_F is the Fermi constant, p_η is the momentum of the η meson and $f_+(q^2)$ the form factor for the $B \to \eta$ transition. With enough data one can measure the shape of $f_+(q^2)$ but the normalization, $\Gamma_{theory} = \Gamma/|V_{ub}|^2$, has to be taken from theory. In terms of the branching fraction $\mathcal{B}(\mathcal{B}^+ \to \eta\ell^+\nu)$ times the total B decay width, we may write

$$|V_{ub}| = \sqrt{\frac{\mathcal{B}}{\tau_B \Gamma_{theory}}} , \tag{2.8}$$

where τ_B is the B lifetime, and Γ_{theory} depends on the from factor model used.

Chapter 3

The *BABAR* Detector

3.1 The PEP-II Collider

As mentioned in the introduction the *BABAR* detector was build to study decays of B meson pairs. The B meson pairs are produced by the PEP-II collider which is shown in Figure 3.1. The PEP-II collider is an e^+e^- collider designed to operate at the center-of-mass energy of 10.58 GeV, which is the mass of the $\Upsilon(4S)$ resonance. The collider is an asymmetric collider which consists of a pair of storage rings and collides a 9.0 GeV electron beam with a 3.1 GeV positron beam. To steer and focus the beams, dipole and quadrupole magnets are used. The position at which the electron beam collides with the positron beam is called the interaction point (IP).

3.2 The *BABAR* Detector

The *BABAR* detector consist of five sub-detector components shown in Figure 3.2, each of which provide complementary information about the final state particles produces
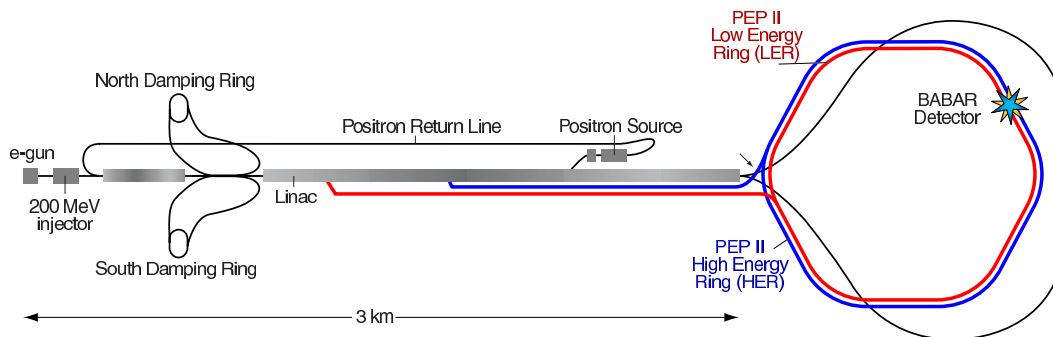
Figure 3.1: The Stanford linear accelerator and the PEP-II storage ring at SLAC in Menlo Park, USA. The *BABAR* detector is located at the upper right corner of this figure.
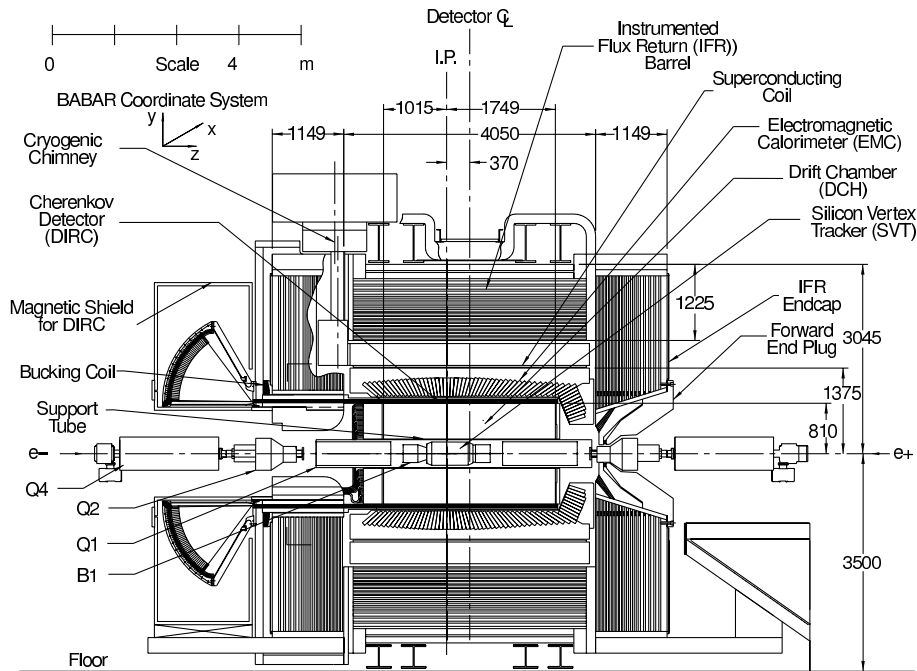
Figure 3.2: Schematic view of the longitudinal axis of the *BABAR* detector. The detectors from the innermost to the outermost detector: silicon vertex detector, drift chamber, Cherenkov radiation detector, electromagnetic calorimeter, instrumented flux return. The superconducting coil is located between the electromagnetic calorimeter and the instrumented flux return. The 9 GeV electron beam enters from the left, the 3.1 GeV positron beam enters from the right.

in the B meson decays. In the following sections a description of each sub-detector component is given, starting from the innermost detector. Further informations about the *BABAR* detector can be found in [12].

3.2.1   Silicon Vertex Detector

The silicon vertex detector (SVT) has been designed to precisely reconstruct charged particles near the interaction point. It also provides a measurement of ionization loss dE/dx. The detector layout is depicted in Figure 3.3.

The detector consist of five layers of double sided silicon strips sensors. On the one side of the sensors the readout strips run parallel to the beam pipe, on the other side they run transverse to the beam pipe. This allows spacial measurement of the track trajectory and angle measurements with high resolution. The achieved spacial resolution various from 20 to 40μm depending on the angle of the track. The mean dE/dx resolution for minimum ionizing particles sampled over the five layers is about 14%.

The three innermost layers provide position and angle information which are im-

10 cm
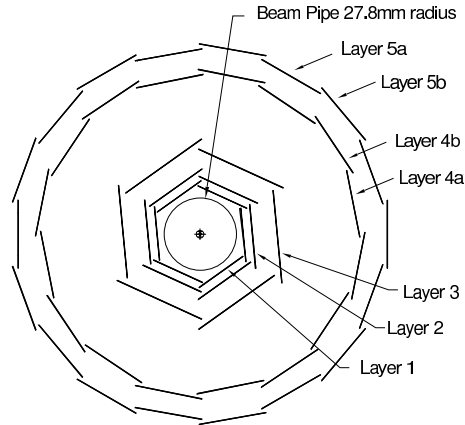
Figure 3.3: Front view of the silicon vertex detector. The six-fold symmetry of the three innermost layers and the sixteen-fold symmetry of the two outer layers can be seen.
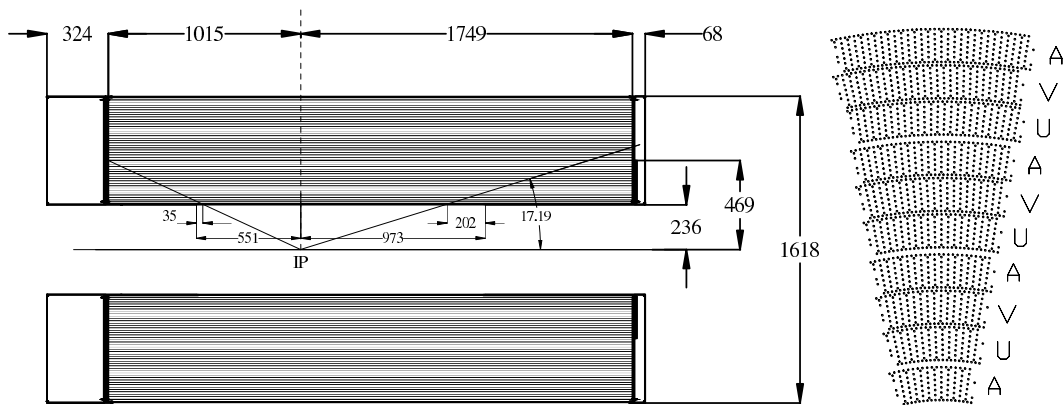
Figure 3.4: Schematic view of the longitudinal axis of the drift chamber. The pattern of the axial and stereo (U,V) layers can be seen on the right.

portant for the measurement of secondary vertices of B meson decays. The fourth and fifth layers are arched shaped to increase the solid angle coverage. The detector covers a polar angle range of $20°$ to $150°$.

3.2.2   Drift Chamber

Precise measurements of momentum and trajectory of charged particles and the measurement of the ionization loss dE/dx is the main purpose of the drift chamber (DCH). The ionization loss measurement is important for the identification of particles up to momenta of 700MeV/c. Reconstruction of decay vertices of long lived particles such as K_S^0 is also possible. The detector layout is depicted in Figure 3.4.

The drift chamber is a 280cm long multi-wire chamber with an inner radius of $r_i =$23.6cm and an outer radius of $r_o =$80.9cm. Aluminum end plates terminate the
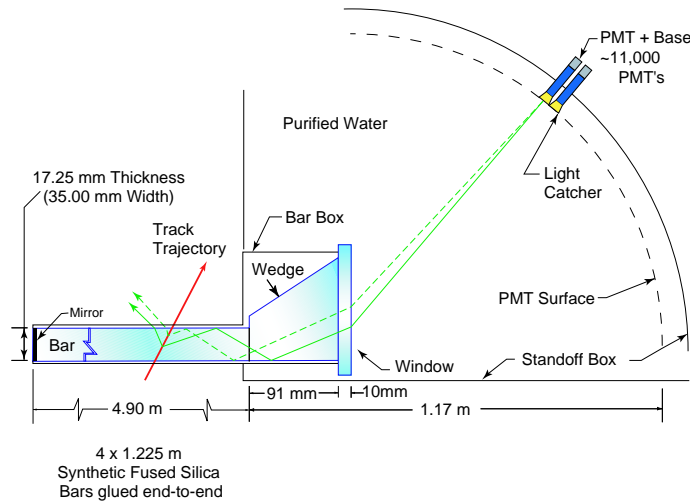
Figure 3.5: The working principle of the Cherenkov radiation detector is illustrated. The light emitted by the particle traversing the Cherenkov radiation detector is internally reflected until it reaches the waterfilled readout reservoir and is detected by the photomultipliers (PMT).

chamber on each side equipped with the readout electronics for the wires. The gas is a mixture between helium and iso-butane in a ratio of 80:20. 40 layers of hexagonal cells are formed by the field wires with a sense wire in the middle of each cell. Wires in 24 of the 40 layers have a slight angle in respect to the beam pipe (z-axis) to gain spacial resolution (stereo layers). The remaining layers have an axial alignment with the beam pipe (axial layers). All sub-detectors apart from the outer most detector (instrumented flux return) are embedded in a 1.5T superconducting solenoid. The magnetic field bends charged tracks and is the basis of the momentum determination in the drift chamber. The average resolution for a single track is 125μm. The resolution in transverse momentum measurements is $\sigma_{p_t}(p_t) = (0.13\pm0.01)\% + (0.45\pm0.03)\%$.

3.2.3   Cherenkov Detector

Charged particle identification especially pion, kaon and proton discrimination is the main task of the Cherenkov radiation detector (DRC). The detector layout is depicted in Figure 3.5.

The Cherenkov radiation detector consist of bars of synthetic fused-silica arranged in a 12-sided polygonal barrel around the drift chamber and an array of 10752 photomultiplier tubes. Cherenkov light is emitted if a particle travels with $v > c$, where v is the speed of the particle and c the speed of light in the material traversed by the particle. The Cherenkov light emitted in the synthetic fused-silica bars is guided by the bars to the photomultipliers in such a way that the angle with which the light was emitted by the particle is retained. Measuring the angle of the light (Cherenkov angle θ_C) gives information about the speed with which the particle traversed the Cherenkov radiation
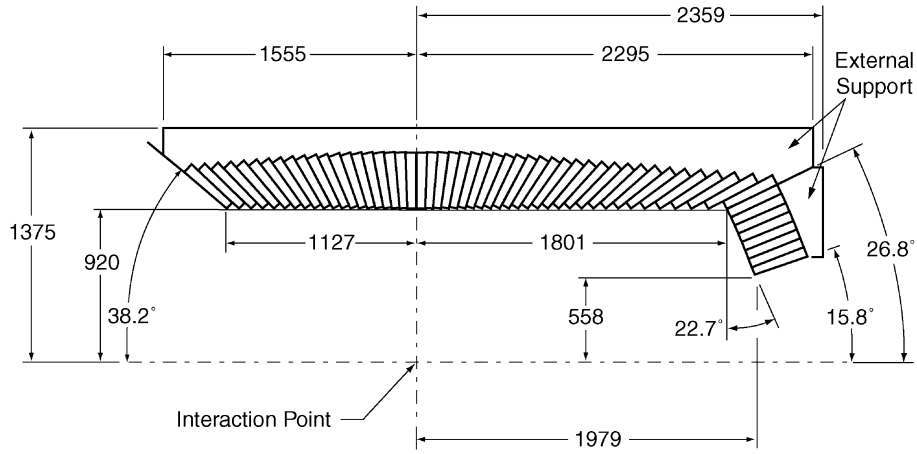
Figure 3.6: Longitudinal view of the top half of the electromagnetic calorimeter. One can see the the crystals which span a polar angle range of $15.8°$ to $141.8°$.

detector (Equation 3.1) and with knowledge about the momentum of the particle (e.g. from a dE/dx measurement in the drift chamber) one can deduce the particles mass which is equivalent with its identity. Equation 3.1 relates the Cherenkov angle (θ_C) with the speed of the particle ($\beta = \frac{v}{c}$)

$$cos\theta_C = \frac{1}{\beta n} \tag{3.1}$$

where n is the diffraction index of the material traversed by the particle.

3.2.4 Electromagnetic Calorimeter

The electromagnetic calorimeter (EMC) measures the position and energy of photons and leptons and information about the shapes of the electromagnetic showers is used to discriminate hadrons and identify leptons. The detector layout is depicted in Figure 3.6.

It consist of a cylindrical barrel which contains 48 rings of 120 Thallium-doped Cesium Iodide crystals. The conical end cap is build with rings of 120, 100, and 80 crystals each. The fine segmentation provides a very fine angular resolution of the order of a few mrad. The detector covers an polar angle range of $15.8°$ to $141.8°$. The azimuthal coverage is $360°$. The energy range in which the electromagnetic calorimeter has good energy and angular resolution stretches from 20MeV to 9GeV. Silicon photodiodes mounted to the end of each crystal detect the light emitted in each crystal.

A electromagnetic shower spreads over a number of crystals and forms a so-called cluster. From the shape of these clusters one can deduce information about the identity of the showering particle. The overall energy resolution $\frac{\sigma_E}{E}$ is

$$\frac{\sigma_E}{E} = \frac{(2.32 \pm 0.30)\%}{4\sqrt{E}} + (1.85 \pm 0.12)\% \tag{3.2}$$

where E (GeV) is the deposited energy and the first term is due to electronic noise, beam background and statistical fluctuations in the scintillation photon yield and the second term is due to leakage and absorption. The angular resolution is

$$\sigma_\theta = \sigma_\phi = (\frac{3.87 \pm 0.07}{\sqrt{E}} + 0.04)\text{mrad} \qquad (3.3)$$

where E (GeV) is the deposited energy. This results in an angular resolution of 12mrad at low energies and 3mrad at high energies.

3.2.5   Instrumented Flux Return

The outermost detector sub-system is the instrumented flux return (IFR) which allows neutral hadron (primarily K_L^0 and neutrons) and muon identification.

  The instrumented flux return uses the steel of the magnet as hadron absorber. Single gap resistive plate chambers are installed in the gaps of the segmented steel of the barrel and its end doors. These resistive plate chambers detect ionizing particles via capacitive readout strips.

3.3   Reconstruction

A description of the reconstruction of tracks, clusters and the connected identification of particles in the *BABAR* experiment is described elsewhere, e.g. [13], [14]. A description of the hadron and lepton reconstruction for this analysis and the treatment of the neutrino is discussed in Chapter 5.

Chapter 4

Data and Monte Carlo Samples

4.1 Data Sample

The data included in this analysis corresponds to an integrated on-peak luminosity of 215 fb^{-1} or 225 million $B\bar{B}$ events. The data has been recorded with the *BABAR* experiment at the Stanford Linear Accelerator Center in Menlo Park, California, USA. Data taken from 1999 till 2005 are included in this analysis. Details of the specific runs are given in Table 4.1.

Data are taken at two different center of mass energies (E_{cms}), E_{cms} equal to the $\Upsilon(4S)$ resonance energy ($\sqrt{s}$=10.58GeV, on-peak data) and E_{cms} equal to $40\,\mathrm{MeV}$ below the $\Upsilon(4S)$ resonance (off-peak data). In greater than 96% of the times the $\Upsilon(4S)$ resonance decays into $B\bar{B}$ pairs [15]. At center of mass energies below the $\Upsilon(4S)$ resonance the energy lies below the threshold for B-meson production, but continuum events such as $e^+e^- \rightarrow q\bar{q}$ or $e^+e^- \rightarrow \ell^+\ell^-$ are still produced. Since the continuum events are also present at the $\Upsilon(4S)$ resonance and form one of the background sources the off-peak data are used to study the continuum background but the off-peak data are not included in the analysis.

	$\int \mathcal{L}\,[\,\mathrm{fb}^{-1}\,]$	
Data sets	On-peak	Off-peak
Run1	20.72	2.65
Run2	60.92	6.87
Run3	32.28	2.47
Run4	101.07	10.21
Total	214.99	22.20

Table 4.1: Integrated luminosities are shown for each run included, which are obtained using standard *BABAR* tools.

4.2   Monte Carlo Sample

Samples of simulated data are used to study the properties of signal and background, to estimate the shape of the signal and background, and to calculate the signal efficiency. The Monte Carlo data production follows the following three steps:

1. Generation of events according to cross section, kinematic properties and decay branching fraction.

2. Simulation of the interaction of particles with the detector.

3. Reconstruction of the tracks and clusters produced in the detector. The same reconstruction is used for simulated events as well as data.

4.2.1   Signal Decay

Simulated samples of exclusive $B^+ \to \eta \ell^+ \nu$ decays were generated with a flat q^2 spectrum[1] (FLAT-Q2 model). Because nature does not produce a flat q^2 spectrum the q^2 spectrum is reweighted using the Light Cone Sum Rule calculation for the $B \to \eta l \nu$ decay [5].

4.2.2   Possible Background Decays

Exclusive Semileptonic Background Decays

The exclusive charmless semileptonic background includes samples of $B^+ \to \pi^0 \ell^+ \nu$, $B^0 \to \pi^- \ell^+ \nu$, $B^+ \to \rho^0 \ell^+ \nu$, $B^0 \to \rho^- \ell^+ \nu$, $B^+ \to \omega \ell^+ \nu$, and $B^+ \to \eta' \ell^+ \nu$ decays all of which are also generated using the FLAT-Q2 model. It is reweighted using the Light Cone Sum Rule calculation for the exclusive samples [5].

Inclusive Semileptonic Background Decays

An inclusive sample of non-resonant charmless background decays are generated with a smooth hadronic mass spectrum according to the triple differential decay rate $d\Gamma/(dx/dz/dq^2)$ defined by de Fazio and Neubert (DFN) [11]. The inclusive sample is reweighted in bins of q^2, the lepton energy E_l in the $\Upsilon(4S)$ frame, and the hadron mass m_X. This works such that the weighted combination of the non-resonant and resonant decay samples corresponds to the measured E_l and q^2 spectrum for the $B \to X_u l \nu$ decay and the sum of non-resonant and resonant give the total $B \to X_u l \nu$ branching fraction.

$B\bar{B}$ Background

$B^+ B^-$ and $B^0 \bar{B}^0$ have been produced where the B meson is allowed to decay to any mode.

---

[1]The variable q^2 is the four momentum transferred in the decay of the W-boson ($q^2 = p_l + p_\nu$) and a flat distribution in q^2 means that the amount produced over the whole q^2 spectrum is the same.

Continuum Background

Continuum background is simulated for $e^+e^- \rightarrow q\bar{q}$ with $q = u, d, s, c$. The fragmentation of the quark is performed by JETSET [17]. Pure QED processes such as Bhabha scattering or two-photon processes are not included in this simulation as they can be easily removed from the data.

Chapter 5

Signal Reconstruction

Since always two B meson are produced in a $\Upsilon(4S)$ decay, there are two completely different approaches for their reconstruction possible. One possibility is to first reconstruct one B meson and then look into the semileptonic decay of the other B meson. Reconstructing signal $B \rightarrow X_u \ell \nu$ decays from the decay particles of both B mesons is one method. Analyses using the former technique are called "tagged" analyses because by reconstructing the momentum, flavor, and charge of one B meson one can predict the quantities of the second B meson and thus assign (or tag) these quantities to the second B meson. Analyses using the later technique are referred to as "untagged" analyses. The advantage of untagged analyses is that one has a much larger data volume because one can use the whole data volume of B meson pair decays whereas tagged analyses use only B meson pair decays where one of the B mesons has been reconstructed. The disadvantage of untagged analyses is that one has much more background. Thus using an untagged analysis versus a tagged analysis is a trade-off between low purity but high efficiency (untagged) and high purity but low efficiency (tagged).

This untagged analysis is based on the same analysis framework as used for a previous untagged analysis covering the decays $B^+ \rightarrow \pi^0(\pi^-, \rho^0, \rho^-)\ell^+\nu$ performed by group C at SLAC [2]. This thesis studies for the first time the decay $B^+ \rightarrow \eta(\rightarrow \gamma\gamma)\ell^+\nu$ with *BABAR* in $B\bar{B}$ events without tagging of the other B meson.

5.1 Implementation of the $B^+ \rightarrow \eta(\rightarrow \gamma\gamma)\ell^+\nu$ decay and Other Decays

Because with the already existing analysis software one could only analyze $B \rightarrow \pi\ell\nu$, $B \rightarrow \rho\ell\nu$ and $B \rightarrow \omega\ell\nu$ decays, the main goal of the first part of this thesis was to include the possibility to analyze the $B \rightarrow \eta\ell\nu$ decay. These changes were made general and not specific to the $B \rightarrow \eta\ell\nu$ mode. Now one can analyze semileptonic decays where the signal hadron decays into three hadrons (or up to seven hadrons) or where the hadron decays into hadrons which are not pions. Studies of those decays

(apart from the three decays mentioned above) were not available before the changes.

Studies which are already using or will use these changes in the near future include the analysis of the following decays:

1. Studies of the decays $\eta \to \gamma\gamma$ (this analysis) and $\eta \to \pi^+\pi^-\pi^0$.

2. Studies of the decays $B \to \eta'(\to \rho\gamma)\ell\nu$, $B \to \eta' \to \eta(\to \gamma\gamma)\pi^+\pi^-\ell\nu$, or $B \to \eta' \to \eta(\to \pi^-\pi^+\pi^0)\pi^+\pi^-\ell\nu$.

3. Studies of the decay $B \to \omega(\to \pi^+\pi^-\pi^0)\ell\nu$.

During the implementation studies of the $\eta \to \gamma\gamma$ decay were performed, some of which are shown in Section 5.6.

The following section describes the reconstruction of the signal decay.

5.2   Charged Lepton Identification (e, μ)

The charged lepton is the characteristic of a semileptonic decay and thus plays a central role in the reconstruction. Both electrons and muons are reconstructed as signal leptons.

Due to their charge both electrons and muons are identified through their electromagnetic interaction in the silicon vertex detector, the drift chamber and the electromagnetic calorimeter. But whereas electrons loose all their energy in the electromagnetic calorimeter muons traverse the detector as minimum ionizing particle and leave a track in the muon detector.

Leptons are selected with the following selection criteria:

- The leptons are taken from a list (GoodTrackLoose **??**) in which tracks are collected with certain requirements such as $p_t > 0.1 GeV/c$ and the number of associated drift chamber hits is $N_{DCH} \geq 12$.

- The lepton polar angle of the leptons must lie between 0.41< θ_l <2.37 rad (laboratory frame), which corresponds to the acceptance of the silicon vertex detector, drift chamber and and excludes the not well calibrated backward region of the electromagnetic calorimeter.

- The lepton momentum in the Y(4S) frame must be above 1 GeV to exclude most secondary leptons[1] which have lower momenta than primary leptons from $B^+ \to X\ell^+\nu$ decays.

To identify electrons as electron and muons as muons standard *BABAR* criteria (selectors) are used. Selectors combine information from various detectors. For the electrons identification a likelihood selector (electronLHselector, [19]) is used based on the following variables:

---

[1]Primary leptons: Leptons which originate from the B meson (($B \to \pi^+\ell\nu$)). Secondary leptons: Leptons which originate from the decay particles of the B meson ($B^+ \to \bar{D}^0(\to K^+\ell^-\nu)\pi^+$).

- the specific energy loss in the drift chamber, dE/dx,

- the Cerenkov angle and the number of photons measured in the DIRC, θ_C, N_γ,

- the ratio of the energy deposited in the electromagnetic calorimeter and electron momentum in the laboratory momentum, E_{cal}/p_{lab},

- the number of crystals in the electromagnetic calorimeter cluster, N_{cry}, and a parameter which describes the lateral shape of the in the calorimeter deposited energy, LAT, and

- the azimuthal distance between the centroid of the electromagnetic calorimeter cluster and the impact point of the track on the electromagnetic calorimeter, $\Delta\Phi$.

For muons the selection is based on a Neural Net selector (`muonNNTightSelector`, [20]) which combines information of the following quantities:

- the energy deposited in the electromagnetic calorimeter, E_{cal},

- the number of IFR hit layers in a cluster, N_L,

- the "continuity" of the track in the IFR, which is defined as $T_C = N_L/(L-F+1)$ and L and F refer to the first and last layer of the IFR with a hit, T_C,

- the $\chi^2/d.o.f.$ of a fit to the IFR hits, χ^2_{fit}, and $\chi^2/d.o.f.$ of the IFR hit strips in the cluster with respect to the track extrapolation, χ^2_{mat},

- the average number of IFR strip hits per layer, $\bar{m}$, and its standard deviation, σ_m, and

- the number of interaction lengths the track penetrated through the detector, λ_{meas}, and the difference between the expected interaction length of the track in the muon hypothesis and the measured interaction lengths, $\Delta\lambda = \lambda - \lambda_m eas$.

- The muon candidates must also fail the criteria for a kaon.

5.3   Neutrino (ν_e, ν_μ)

The neutrino leaves no trace in the detector because it interacts only weakly. It is therefore identified indirectly by using the missing energy and momentum in the event. If the neutrino is the only undetected particle in the event the missing energy (E_{miss}) and the missing momentum ($\vec{p}_{miss}$) are the energy and the momentum of the neutrino ($\vec{p}_\nu$ and E_ν). Equation 5.1 then gives the neutrino four-vector:

$$(\vec{p}_\nu, E_\nu) = (\vec{p}_{miss}, E_{miss}) = (\vec{p}_{beams}, E_{beams}) - (\sum_i \vec{p}_i, \sum_i E_i), \qquad (5.1)$$

where i denotes all tracks in the events and E_{beams} and $\vec{p}_{beams}$ refer to the beam energy and beam momentum. All track and cluster quantities are used in the laboratory frame. To eliminate inaccurate tracks and clusters but keep as much of the event as possible rather loose track and cluster requirements are used.

5.4 Hadron Reconstruction (η)

Decays of the η hadron with sizable branching fraction are $\eta \to \gamma\gamma$ (39.4%), $\eta \to \pi^0\pi^0\pi^0$ (32.5%) and $\eta \to \pi^+\pi^-\pi^0$ (22.7%). This analysis analyses the decay $B \to \eta\ell\nu$ where the η meson decays into two photons because it is the decay with the largest branching fraction. A "Simple Composition" list[2] is used for the $B \to \eta\ell\nu$ candidates and the reconstruction of the η meson as a pair of two photons has the following requirements (Table 5.1):

E_γ A minimum energy of signal photons is required to eliminate low energetic background photons.

$M_{\gamma\gamma}$ The invariant mass of the two photons must satisfy a range around the PDG η meson mass value ($M_\eta^{PDG} = (547.51 \pm 0.18)MeV$)

p_η^{lab} The minimum momentum of the hadron in the laboratory frame is required.

LAT A parameter which describes the lateral shape of the in the calorimeter deposited energy.

Variable	Value
$E_{lab,\gamma}$	$0.10 GeV < E_\gamma$
$M_{\gamma\gamma}$	$0.47 GeV < M_{\gamma\gamma} < 0.62 GeV$
$p_{lab,hadron}$	$0.20 GeV < p_{hadron}^{lab}$
LAT	$0.0 < LAT < 0.8$

Table 5.1: Selection criteria for the η meson **??**.

5.5 Test of η Reconstruction

To understand the η reconstruction one wants to look at variables exclusively from a $B^+ \to \eta(\to \gamma\gamma)\ell^+\nu$ decay. For this purpose one uses only the simulated $B^+ \to \eta(\to \gamma\gamma)\ell\nu$ Monte Carlo sample.

To compare generated (true) decays with the reconstructed decays

---

[2]Simple Composition list ('etaDefault'): A candidate list in which two photons or three pions ($\pi^+\pi^-\pi^0$) are reconstructed to an η candidates

1. several new tools were introduced with which one can apply different selections and different form factor calculations, and

2. new variables were added in the analysis ntuples to study the origin of the background.

The following paragraph will explain the newly introduced variables and summarize the results from the studies made.

Reconstructed and true final state particle: The used candidate list[3] includes two different final states of the η meson ($B^+ \rightarrow \eta(\rightarrow \gamma\gamma)\ell\nu$ and $B^+ \rightarrow \eta(\rightarrow \pi^+\pi^-\pi^0)\ell\nu$), and a way to distinguish between the two decay channels is needed. New defined variables give information what final state particles from the hadron decay were reconstructed and what true final state particle were present. A third new variable can be used to find out if every particle in the decay chain has a truth match.

True Photon and Eta ID These variables give information about the true identity of the photons and their mothers. Again it was set up so that not only one can study $B^+ \rightarrow \eta(\rightarrow \gamma\gamma)\ell\nu$ decays but any semileptonic decay included in the Monte Carlo Simulation.

Further variable which were not present but were needed for these studies.

$E_{daughter}$: The energy of the daughter photons.

$N_{daughters}$: The number of hadron daughters were limited to two daughters. The new limit is six daughters and should cover most semileptonic decays.

As mention before all these new variables are set up in a way so that not only one can analyze $B^+ \rightarrow \eta(\rightarrow \gamma\gamma)\ell\nu$ decays but also most other semileptonic decays with one signal hadron.

Using these variables the origin of the background was studied. The results (summarized in Table 5.2 and Table 5.3) show that 94.2% of the reconstructed signal photons are true photons and only a small fraction are leptons (1.7%), charged pions (1.9%), or K_L^0 (0.5%). Of those correctly reconstructed photons 59.4% originate from true η mesons but almost 37.7% are from a π^0 decays.

5.6 Kinematic Distributions of the $B^+ \rightarrow \eta(\rightarrow \gamma\gamma)\ell^+\nu$ Decay

Plots of distributions of $B^+ \rightarrow \eta(\rightarrow \gamma\gamma)\ell^+\nu$ Monte Carlo only are shown in Figure 5.2 and Figure 5.3.

---

[3]Simple Composition list "etaDefault"

True identity of signal photons	
True Origin	Number in %
Photon	94.2
Electron (e^- and e^+)	1.7
Charged Pions	1.9
K_L^0	0.5

Table 5.2: The true identity of the reconstructed signal photons in %. Studies made with signal Monte Carlo.

True Identity of Photons Mother Particle	
η	59.4 %
π^0	37.7 %

Table 5.3: The true identity of the mother particle of the reconstructed photons. Mother particles which are not η or π^0 mesons contribute less than 3%. Studies were made with Monte Carlo.

Figure 5.1 shows the invariant mass of the two reconstructed photons. The left plot shows the reconstructed mass of two photons both originating from an η meson. The right plot shows the mass if one of the photons originates from an η meson the other photon comes from a π^0. Only if both reconstructed photons originate from an η meson the mass shows a peak at the η mass. To eliminate photons originating from a π^0 decay a new variable ($m_{\gamma\gamma}^{\pi^0}$) is introduced, which is described in Section 6.2.

Figure 5.2 shows the magnitude of the momenta for the lepton, the neutrino, and the hadron in the center of mass frame (p_l^*, p_{miss}^*, p_h^*) and the polar angle in the laboratory frame ($\theta_l, \theta_{miss}, \theta_{h,}$). The long tail of the missing momentum distribution is due to particle losses.

Comparison of these plots with $B^+ \rightarrow \pi^0(\rightarrow \gamma\gamma)\ell\nu$ decays were done and as expected the lepton momenta from the η decay are slightly lower and hadron momenta for η decay are slightly higher than the corresponding momenta of the π^0 decay. This is due to the heavier mass of the η meson.

Figure 5.3 and Figure 5.4 show the m_{ES} and ΔE distributions as well as the q^2 distribution. A description of these variables is given below. The kinematic variables ΔE and m_{ES} are used in this analysis for consistency checks of a B decay. The q^2 spectrum is important if one measures the q^2 dependence of the form factor. Further studies might want to do this and thus this analysis checked the q^2 spectrum throughout this analysis.

ΔE: ΔE is defined as the difference between the energy of the reconstructed B ($E_{rec.B}^*$) in the center of mass frame and the energy it is expected to have, which
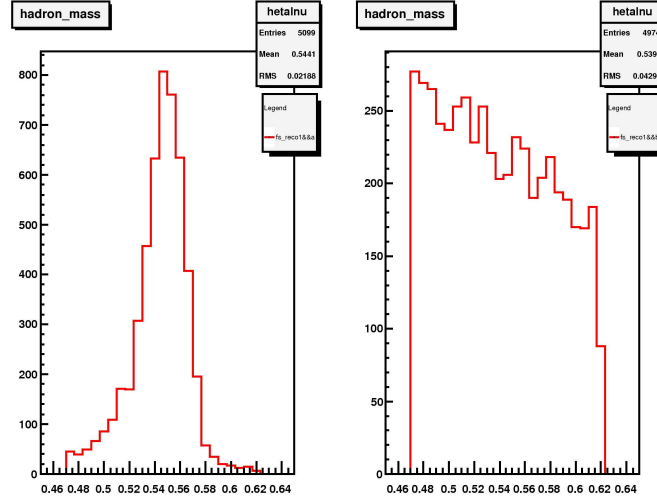
Figure 5.1: Invariant mass of the two reconstructed signal photons. Left: both photons mothers are true η mesons, (right) one is a η and one is a π^0.

is half of the initial energy in the center of mass frame:

$$\Delta E = E^*_{rec.B} - E^*_{beam} \tag{5.2}$$

Correctly reconstructed B decays should peak at zero in this variable, which can be seen in Figure 5.3 which shows the ΔE distribution for signal Monte Carlo.

Energy Substituted Mass, m_{ES}: The mass of the reconstructed B meson with the constrain $\Delta E = 0$ is calculated:

$$m_{ES} = m_{rec.B} = \sqrt{(s/2 + \vec{p}_{rec.B} \cdot \vec{p}_{beam})^2/E_{beam} - \vec{p}^2_{rec.B}} \tag{5.3}$$

Because the reconstructed B energy is replaced with E_{beam} ($\Delta E = 0$ requirement) this variable is called the energy substituted (E.S.) mass, m_{ES}. Correctly reconstructed B decays should peak at the B mass in this variable. Which can be seen in Figure 5.3 where the m_{ES} distribution for signal Monte Carlo is shown.

Throughout this analysis two region are used: the fit region which includes all events which are used in the extraction of the branching fraction (Chapter 7) and the signal region in which a higher signal-to-background ratio is achieved. These regions are defined over cuts in the two variables ΔE and m_{ES}:

fit region The region in which the events must lie to be included in the fit. The values for m_{ES} and ΔE are:

$$|\Delta E| < 0.95 GeV \quad , \quad 5.095 < m_{ES} < 5.295 GeV. \tag{5.4}$$

signal region This region is where most of the signal is located and the signal over background ratio is high. It is used for illustration purposes only:

$$-0.15 < |\Delta E| < 0.25 GeV \quad , \quad 5.255 < m_{ES} < 5.295 GeV \qquad (5.5)$$

signal band Plots of ΔE shown in the signal band have the m_{ES} signal cut ($5.255 < m_{ES} < 5.295 GeV$) applied but not the ΔE signal cut ($-0.15 < |\Delta E| < 0.25 GeV$). Plots of m_{ES} shown in the signal band have the ΔE signal cut applied but not the m_{ES} signal cut.

side band Plots of ΔE shown in the side band have the reversed m_{ES} signal cut applied but not the ΔE signal cut. Plots of m_{ES} shown in the side band have the reversed ΔE signal cut applied but not the m_{ES} signal cut.

Four Momentum Transferred, q^2: As mentioned in Chapter 4, q^2 is the four momentum transferred squared of the virtual W boson (m_W^2), which can be express as the sum of the four momenta of lepton (p_l) and neutrino (p_ν) or the difference between the B meson four momentum (p_B) and the hadron four momentum (p_X):

$$q^2 = m_W^2 = (p_l + p_\nu)^2 = (p_B - p_X)^2. \qquad (5.6)$$

q^2 varies between zero and q_{max}^2, which can be calculated by subtracting the η meson mass from the B meson mass ($(M_B - M_\eta)^2 = 22.4 GeV$).

Corrected q^2 Spectrum, q_{corr}^2: E_{miss} and $\vec{p}_{miss}$ dominates the resolution measured $\vec{p}_{miss}$ is corrected by requiring $\Delta E = 0$ and $m_{ES} = M_B$. In Figure 5.5 one can see the large improvement in the resolution of q^2 due to these constrains, where the black line is the uncorrected q^2 resolution and the red line is the corrected q^2 resolution. q_{reco} refers to the q^2 value which was reconstructed and q_{true} refers to generated q^2 value. The shown q^2 resolution shows clearly that an improvement is achieved with the corrected q^2 variable. A two Gaussian fit to the corrected q^2 resolution is performed which is shown in Figure 5.5 (right), where p_2 and p_5 refer to the mean of the two Gaussian curves and p_1 and p_4 to their widths.
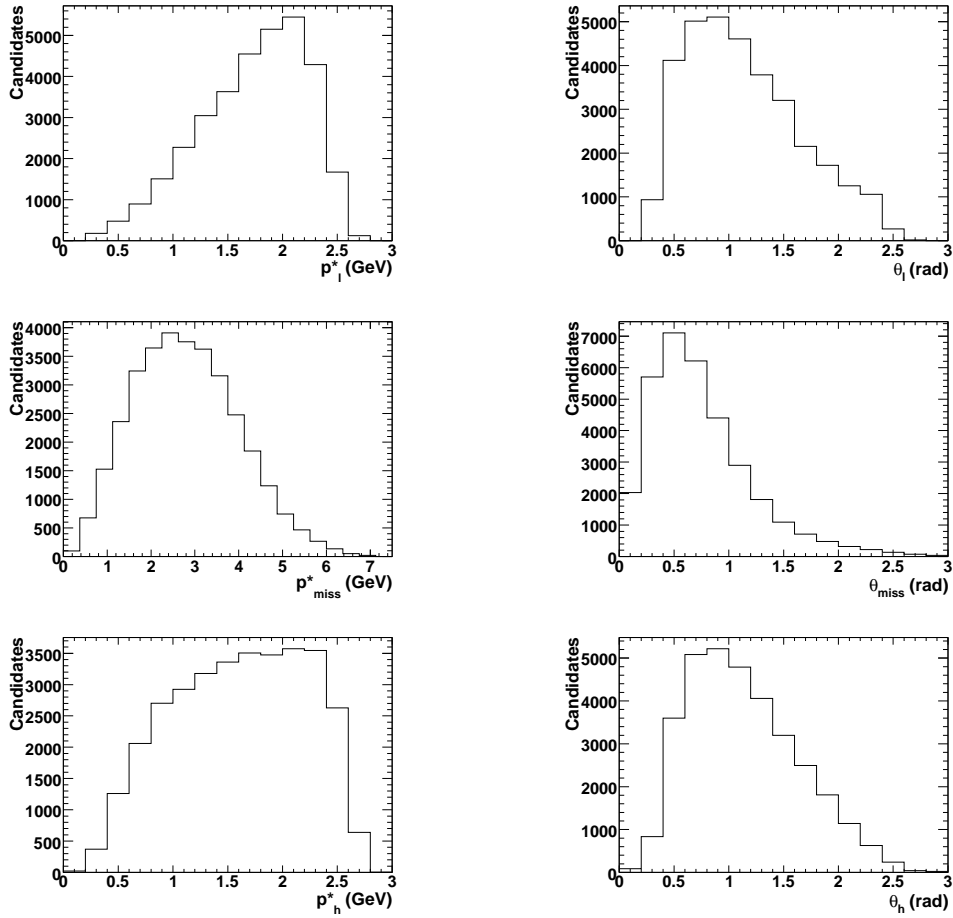
Figure 5.2: Momentum in the center of mass frame and its polar angle of lepton, neutrino and hadron for $B^+ \to \eta(\to \gamma\gamma)\ell^+\nu$ Monte Carlo events.
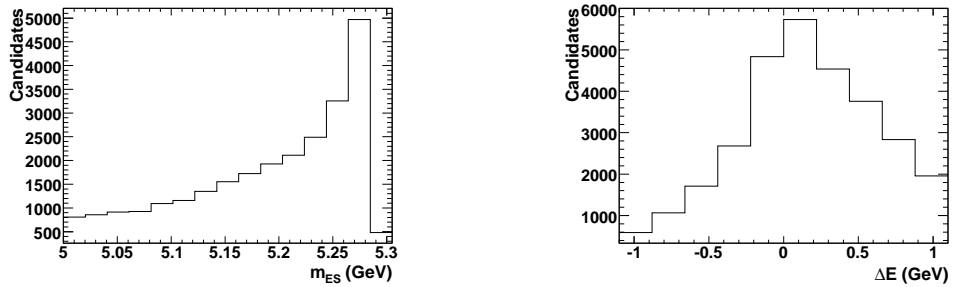
Figure 5.3: m_{ES} and ΔE distributions for signal Monte Carlo.
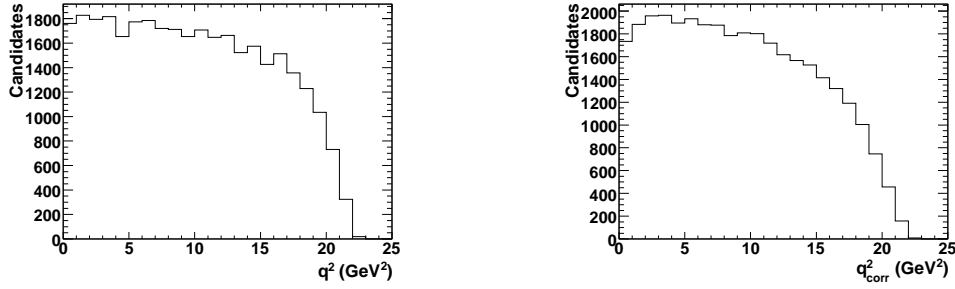
Figure 5.4: Q^2 spectrum uncorrected (left) and corrected (right) for signal Monte Carlo.
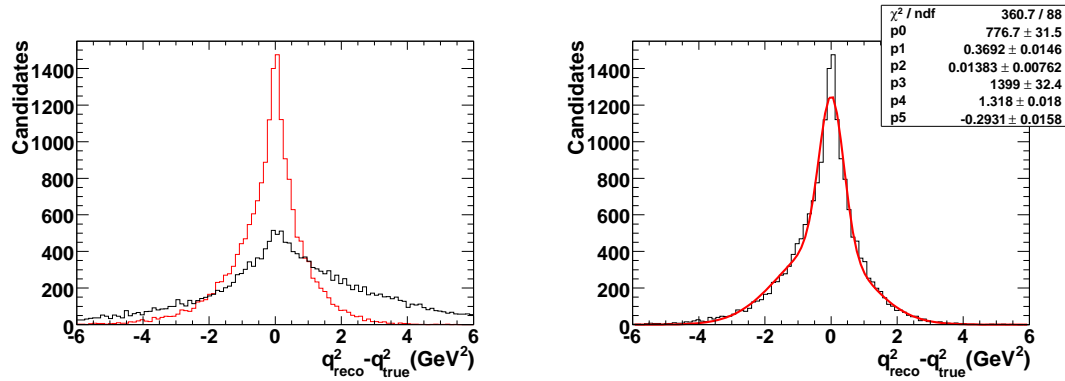
Figure 5.5: q^2 resolution: (left) the difference of the reconstructed q^2 and the true q^2 value (black, $q^2 - q^2_{true}$) and the difference of the q^2_{corr} and the true q^2 value (red, $q^2_{corr} - q^2_{true}$). The right plot shows a fit with two Gaussian to the $q^2_{corr} - q^2_{true}$ distribution.

Chapter 6

Selection of Signal Candidates

6.1 Signal and Background Classification

In Chapter 5 an overview of the background constributions was given. This chapter discusses in detail the signal and background classification as used throughout the analysis.

The classification procedure starts with the origin of the charged lepton, since electrons and muons can be reliably reconstructed and are the most characteristic signature of semileptonic decays. The simulated data are subdivided into the various sources: first it is tested if the lepton comes from a B decay. If not, the source is classified as continuum background. In both cases a check is performed if the lepton was a fake, i.e. misidentified, lepton or a true lepton. In case the signal lepton comes from a B decay Figure 6.1 describes the procedure: if it is a true lepton it is further subdivided on the basis of which B decay it originated from.

The reconstructed lepton is combined with a reconstructed η meson and this combination is called a "Y candidate". In data one does not know where the candidate really came from. Thus the sum of the various Monte Carlo sources, scaled to the correct integrated data luminosity, is compared with data.

6.1.1 Signal

The simulated signal decays are subdivided into two classes. The first one comprises candidates which are fully "truth-matched" [1]. The second is called "combinatoric" signal[2]. Because both classes of signal candidates come from true $B^+ \to \eta(\to \gamma\gamma)\ell^+\nu$ decays, for the branching fraction measurement no distinction is made between the

---

[1]Truth-matched signal denotes signal decays where all final-state particles of the $B^+ \to \eta\ell^+\nu$ decay are correctly identified and correctly associated ("matched") with the corresponding generated ("truth") particles.

[2]Combinatoric signal denotes signal decays where the lepton comes from an $B^+ \to \eta\ell^+\nu$ decay, but the hadron or some of the hadron's decay products do not.

Reconstructed lepton

is misidentified hadron

fake lepton $B\bar{B}$

does not originate from primary semileptonic B decay

$b \rightarrow other$

originates from primary $b \rightarrow cl\nu$ decay

$b \rightarrow cl\nu$

originates from primary $b \rightarrow ul\nu$ decay other than signal channels

$b \rightarrow ul\nu$

originates from a signal channel other than a reconstructed mode or its isospin conjugate

crossfeed

originate from signal decay

real signal

originates from signal decay but hadron does not

combinatoric signal

Figure 6.1: Classification procedure for candidates from simulated $B\overline{B}$ events. This figure is taken from [18].

two cases. It should be noted that for the combinatoric signal the reconstruction of the neutrino is still reliable as it is reconstructed from the missing energy and momentum.

6.1.2 Background Decays

Continuum background:
  Due to the relatively small amount of off-peak data, the $e^+e^- \to q\bar{q}$ Monte Carlo simulation, where $q = u, d, s, c$, is used to estimate this background. This analysis relies on Monte Carlo simulation both for the study of background suppression and to estimate the shapes of continuum background distributions.

  This background is divided into two classes based on the reconstructed lepton being a true or a fake lepton. True leptons often come from $e^+e^- \to c\bar{c}$ events where one c-quark decays semileptonically. Other continuum background sources such as Bhabha scattering or two-photon processes are not simulated, but their contributions are expected to be negligible. The contribution of lepton pair production can also be neglected in this analysis.

Background from non-signal B-decays:

  $B \to X_u \ell \nu$: The charmless semileptonic background consists of the exclusive $B \to X_u \ell \nu$ ($X_u = \pi, \pi^0, \rho, \rho^0, \omega, \eta'$) and the non-resonant $B \to X_u \ell \nu$ decays. In the high q^2-region the $B \to X_u \ell \nu$ background is the most problematic because it has similar kinematic properties and the event characteristics are similar to our signal. When the candidate lepton comes from an exclusive $B \to X_u \ell \nu$ decay mode other than the signal mode this background is called "crossfeed".

  $B \to X_c \ell \nu$: The branching fraction of charmed semileptonic decays is much higher than the branching fraction of $B \to X_u \ell \nu$ decays, and charmed semileptonic decays thus constitute the dominant background for this analysis. This background consists of semileptonic decays with $X_c = \bar{D}^0$, $D^*(2007)^0$, D^{**}, and a non-resonant $D^{(*)}\pi$ contribution.

  Other B decay backgrounds: Other B backgrounds are the $B \to other$ source which covers decays where the lepton comes from a secondary decay or is faked by a hadron.

6.2 Definition of Variables

In the following, definitions and descriptions of variables that are used in the selection of $B \to \eta \ell \nu$ candidates and for the suppression of backgrounds are given. These variables can be roughly divided into three categories based on their purpose in the selection:

1. **Neutrino Quality:**

   Missing Momentum, p_{miss} (Figure 6.13): If there is only one missing particle
   in the event, in this case the neutrino, the missing momentum corresponds
   to the momentum of this particle alone. As a sign of a neutrino, a minimum
   missing momentum in the event is required. In addition, events with a
   missing momentum above a maximum allowed value are rejected since
   high missing momenta are more likely for an event with more than one
   missing particle.

   Polar Angle of Missing Momentum, θ_{miss} (Figure 6.13): Due to the asymmet-
   ric beam energies the particles are boosted in the forward direction. The
   detector does not cover a solid angle of 4π and the very forward particles
   cannot be reliably reconstructed. To limit effect of losses due to detec-
   tor acceptance, events where the missing momentum points in the not-well
   covered forward region are rejected.

   Missing Mass squared, M^2_{miss} (Figure 6.14): The M_{miss} variable in semilep-
   tonic decays should be equal to the neutrino mass and thus should be ap-
   proximately zero. Further undetected particles shift this variable away from
   zero.

2. **Event Topology (Continuum Suppression):**

   $B\bar{B}$ events are isotropic in the center of mass frame whereas $e^+e^- \to q\bar{q}$ events
   are "jet-like". Topological cuts are therefore most useful to suppress continuum
   background. Harsh cuts are used to suppress the continuum background.

   Angle between thrust axes, $cos\theta_{Thrust}$ (Figure 6.14): The cosine of the an-
   gle between the thrust axis of the Y-candidate and the thrust axis of the
   rest of the event. A thrust axis $\vec{A}$ from N particles is defined as the vector
   with unit length along which the maximum alignment is found:

$$thrust = |(\frac{\sum_{i=1}^{N} |\vec{A} \cdot \vec{p_i}|}{\sum_{i=1}^{N} \vec{p_i} \cdot \vec{p_i}})| \tag{6.1}$$

   where $\vec{p_i}$ refers to the momentum of the ith particle. The more jet-like
   continuum events have higher values and by rejecting events with large
   values of $cos\theta_{Thrust}$ jet-like can be distinguished from isotropic events.

   Legendre Moment, $L2$ (Figure 6.14): $L2 = \sum_i |\vec{p_i^*}| \cos^2\theta_i^*$ GeV is the sum
   over all track angles squared weighted with the track momenta in the center
   of mass frame, excluding the Y-system (electron and hadron). The angles
   are measured with respect to the thrust axis of the Y-system.

Second normalized Fox Wolfram Moment, $R2$ (Figure 6.14): A Fox Wolfram moment is defined as :

$$R2 = \sum_{ij} |\vec{p_i}||\vec{p_j}|P_l cos\theta_{ij} \qquad (6.2)$$

when the sum is over all final state particles with momenta $\vec{p_i}$ and $\vec{p_j}$ and θ_{ij} the angle between them. P_l refers to the Legendre polynomials of order l: $P_0(x) = 1$ and $P_2(x) = (1/2)(3x^2 - 1)$. $R2$ is the second Fox-Wolfram moments normalized to the 0th moment. A jet-like event has a value close to unity whereas more spherical events have values closer to 0.

3. **Suppression of other Backgrounds:**

cos θ_{BY} (Figure 6.14): θ_{BY} is the angle between the B meson and the Y system (which is the hadron and lepton):

$$\cos\theta_{\mathrm{BY}} = \frac{2E_B E_Y - M_B^2 - M_Y^2}{2|\vec{p_B}||\vec{p_Y}|}. \qquad (6.3)$$

where E_B, M_B, $\vec{p_B}$ and E_Y, M_Y, $\vec{p_Y}$ refer to the energy, the mass and the three-momentum of the B meson and the Y system, respectively. Semileptonic signal decays lie between -1 and 1 (corresponding to physical values for the angle between the B meson and the Y-candidate) and have a radiative tail toward negative values for electrons. Continuum and $B\overline{B}$ backgrounds are more broadly distributed and have values also larger than $|1|$.

N_{tracks} **(Figure 6.15):** The minimum number of tracks required in the event is four tracks. One track comes from the lepton in the $B^+ \rightarrow \eta\ell^+\nu$ decay while it is assumed that the decay of the other B-meson, which most of the time decays hadronically, produces on average at least three charged tracks.

Lepton and Hadron Momentum, p_l^*, p_h^* (Figure 6.13): The dominant background from $B \rightarrow X_c\ell\nu$ decays tends to have lower lepton and hadron momenta due to the larger masses of the charmed mesons compared to the charmless mesons. It is not advisable to apply very harsh kinematic cuts in this analysis in order to measure as much of the available phase space as possible and allow a measurement of the full q^2 spectrum. Nevertheless loose cuts are applied on the lepton and hadron momenta in the center of mass frame and on their sum $|p_l^* + p_h^*|$ at a very early stage in the analysis, as shown in Table 6.2.

Reconstructed η Candidate Mass, $M_{\gamma\gamma}$ (Figure 6.15): If the invariant mass of the two reconstructed photons deviates significantly from the η mass at least one of the photons probably did not originate from an η meson. To exclude those η candidates a 2σ cut around the mean of the Gaussian function fitted to the mass distribution in signal Monte Carlo is made

$(M_{\gamma\gamma}^{FIT} = (545 \pm 0.3)MeV$ with $\sigma = (15.1 \pm 0.3)MeV$; $M_{\eta}^{PDG} = (547.51 \pm 0.18)MeV)$. The fit is shown in Figure 6.2.
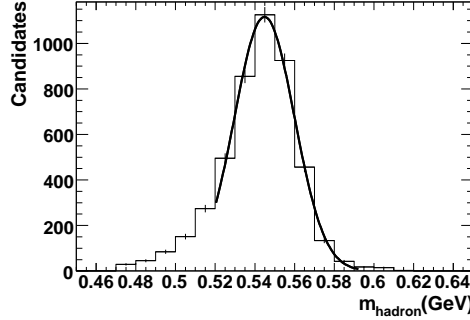
Figure 6.2: Fit of a Gaussian function to the $M_{\gamma\gamma}$ spectrum for signal Monte Carlo data (only correctly reconstructed $B \rightarrow \eta(\rightarrow \gamma\gamma)\ell\nu$) with skim and preselection cuts applied $(M_{\gamma\gamma}^{FIT} = (545 \pm 0.3)MeV$ with $\sigma = (15.1 \pm 0.3)MeV)$. The PDG value of the η mass is $M_{\eta}^{PDG} = (547.51 \pm 0.18)MeV$. Definition of the cuts can be found in Section 6.3.

π^0**Veto, $m_{\gamma\gamma}^{\pi^0}$ (Figure 6.15):** To exclude candidates where one of the reconstructed signal photons comes from a π^0, which occurs frequently in B-decay final states or in continuum events, this new variable is introduced. Each of the two signal photons is combined with all other photons with $E_\gamma > 0.100GeV$ in the event and the invariant mass is calculated. Signal photons are rejected if they are used in the reconstruction of a π^0 candidate. The distribution has a long tail and ends beyond a peak at the η mass. For signal, the tail above the π^0 mass and below the η mass is composed, in part, of combinations of one signal photon with another photon in the event. This might yield an invariant mass closer to the π^0 mass than the η mass. Combinations of signal photons with photons from other hadronic decays or single photons make up the rest of the tail. The peak at the η mass originates from true $\eta \rightarrow \gamma\gamma$ decays where no additional photon $E_\gamma > 0.100GeV$ was present in the event.

6.3   Selection Steps

The total data volume of real and simulated data in Runs 1-4 used in this analysis is of the order of a few hundred Terabytes. Three steps are used to select the signal decay, which are described below. The first two steps (skim and preselection) aim at reducing the size of the data samples by making rough cuts to eliminate background events and at the same time retain most of the signal. The third step consists of stringent cuts with which the final signal selection is done.

6.3.1 Exclusive $B \to X_u \ell \nu$ Skim

The data samples used in this analysis have been selected by an event filter, or a so-called skim, which is specifically designed to select exclusive $B \to X_u \ell \nu$ events and applies loose cuts to eliminate events with characteristics that are clearly different from the wanted signal decay. Details of the implementation of the skim are documented in Reference [22] and the cuts applied by the skim are summarized in Table 6.2. Almost 50% of the $B^+ \to \eta \ell^+ \nu$ signal is kept while 98% of the continuum and 90% of the $B\overline{B}$ background is eliminated. The skim efficiencies for the various signal and background samples are shown in Table 6.1.

	$B^+ \to \eta \ell^+ \nu$	$B \to X_u \ell \nu$	other $B\overline{B}$	$q\bar{q}$
Skim Efficiencies (%)	48.7	42.4	11.0	2.1

Table 6.1: Skim efficiencies for signal and backgrounds.

6.3.2 Preselection

On top of the skim, an additional preselection is applied to further reduce the data volume. The preselection cuts are mainly adopted from the *BABAR* analysis studying the $B \to \pi \ell \nu$ and $B \to \rho \ell \nu$ decays [2].

Figure 6.3 and Figure 6.4 show the data to Monte Carlo agreement for kinematic distribution after the preselection cuts have been applied. These plots show the distribution for electrons and muons separately.

6.3.3 Final Selection

The final signal selection cuts are quite hard cuts targeted at achieving a good signal-to-background ratio, allowing the extraction of the signal branching fractions. The full set of cuts is shown in Table 6.2. Table 6.3 shows the effect of each cut on the signal efficiency and background rate after all other selection cuts have been applied. The total signal efficiency after the full selection amounts to 1.7%. The signal-to-background ratio in the $\Delta E - m_{ES}$ signal region is 0.36. In Figure 6.5 the effect of each selection cut on the q^2 spectrum can be seen.

Preselection for Electrons only
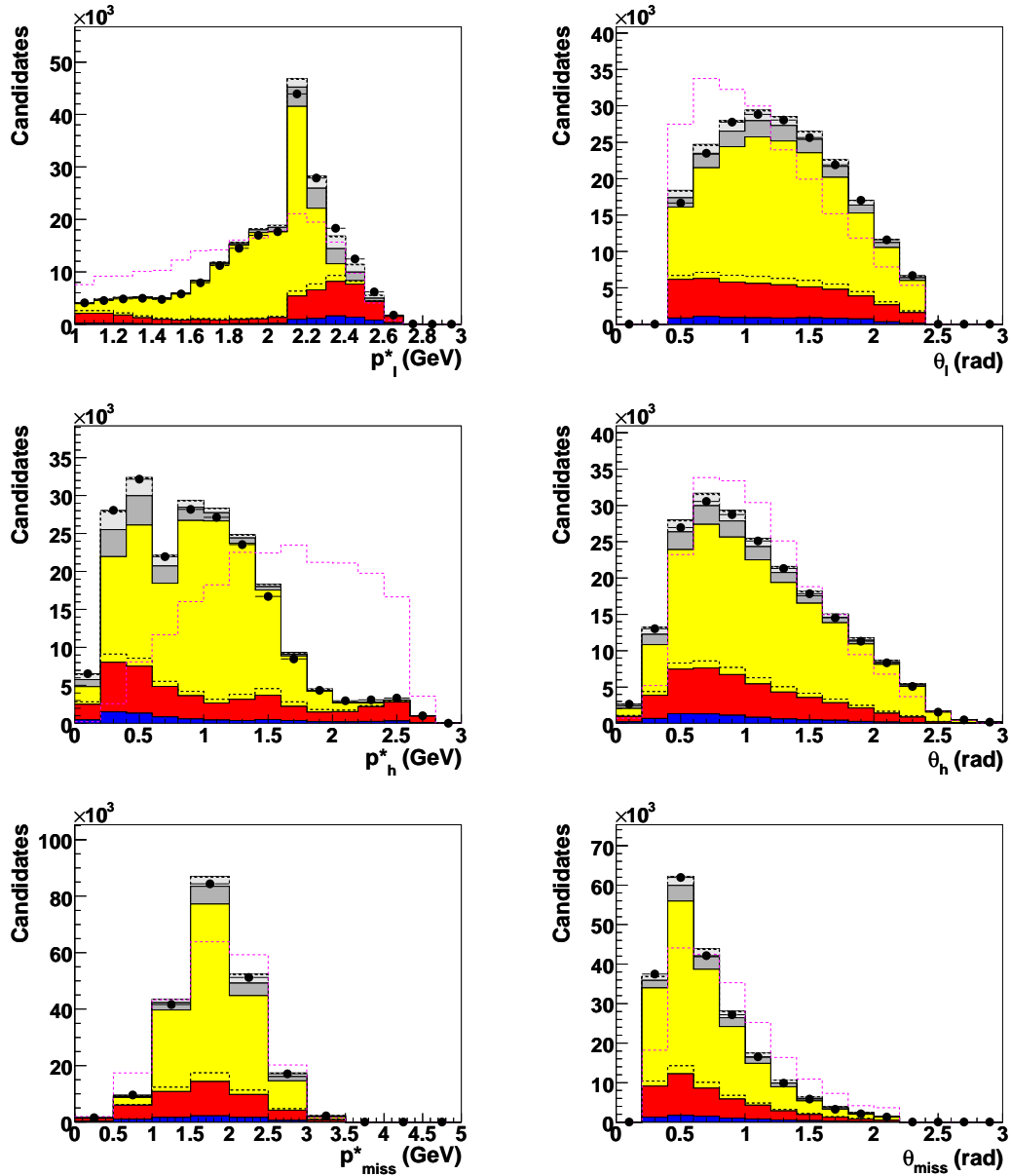
Figure 6.3: Momenta in the center of mass system and polar angles for lepton, hadron and neutrino are shown. Shown are on-peak data and Monte Carlo data for electrons only. Only preselection cuts have been applied The pink dashed line illustrates the signal shape with an arbitrary normalization. A legend can be found in Figure 6.6.
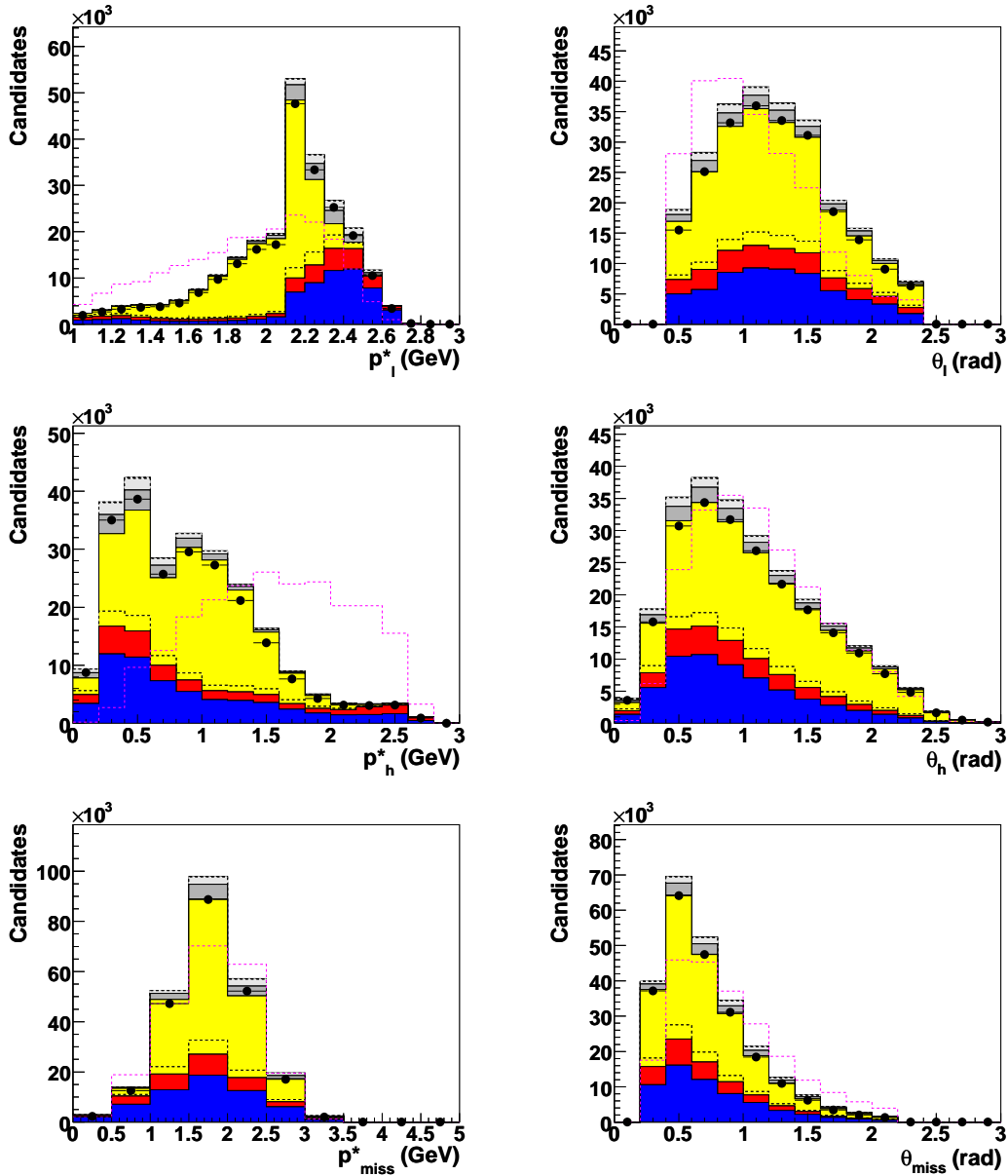
Figure 6.4: Momenta in the center of mass system and polar angles for lepton, hadron and neutrino are shown. Shown are on-peak data and Monte Carlo data for muons only. Only preselection cuts have been applied The pink dashed line illustrates the signal shape with an arbitrary normalization. A legend can be found in Figure 6.6.

Variable	Skim (BAD 740)	Preselection	Final Selection
$R2$	$R2 \leq 0.5$		
$cos\theta_{BY}$	$-1.1 < cos\theta_{BY} < 1.3$	$-1.0 < cos\theta_{BY} < 1.0$	
$p_e^{lab}(p_\mu)$	$\geq 0.5(1.0)GeV$		
θ_l	$0.41 \leq \theta_l \leq 2.54$		
p_h^{lab}			
$p_l + p_h$	$\|p_h^*\| \geq 1.3 \, or \, \|p_l^*\| \geq 2.1 \, or \, \|p_l^*\| + \|p_h^*\| \geq 2.8$ or $\|p_l^*\| + \|p_h^*\| \geq 2.8$		
N_{tracks}		$N_{tracks} > 3$	
ΔE		$\|\Delta E\| < 0.95 GeV$	
m_{es}		$5.095 < m_{ES} < 5.295 GeV$	
q_{corr}^2		$0 < q_{corr}^2$ GeV^2	
$m_{\gamma\gamma}^{\pi^0}$			$0.110 < m_{\gamma\gamma}^{\pi^0} < 0.160 GeV$
M_h		$0.47 < M_h < 0.62 GeV$	$0.50 < M_h < 0.58 GeV$
$L2$		$L2 < 3.0$ GeV	$L2 < 1.7$ GeV
$cos\theta_{Thrust}$	$\|cos\theta_{Thrust}\| < 0.9$		$cos\theta_{Thrust} < 0.6$
M_{miss}^2		$\|M_{miss}^2/2E_{miss}\| < 2.5$ GeV	$M_{miss}^2 < 3.0$ GeV^2
θ_{miss}		$0.3 < \theta_{miss} < 2.2$ rad	$\theta_{miss} > 0.4$ rad
p_{miss}			$0.7 < p_{miss} < 3.0$ GeV
E_γ			$E_\gamma > 0.1 GeV$ GeV

Table 6.2: Summary of cuts used in the skim, the preselection, and the final selection.

6.4 Signal and Background Efficiencies

In Table 6.3 the efficiencies for each selection cut are shown. Cuts on $m_{\gamma\gamma}^{\pi^0}$ and the M_{miss}^2 have the best background suppression. As a reminder the newly introduced $m_{\gamma\gamma}^{\pi^0}$ variable was introduced to suppress photons from true π^0's. Whereas the $m_{\gamma\gamma}^{\pi^0}$ cut has an 62% signal efficiency with a background efficiency of below 31%, the M_{miss}^2 cut only retains 85% of the signal with a background efficiency of around 60% for B decay background and 15% for the continuum background. The harsh cut on M_{miss}^2 is necessary to exclude events in which further undetected particle which shift the missing mass to high values are present. Other signal efficiencies lie between 80% and 97% with background efficiencies between 60% and 95% for B decay background and 13% and 20% for continuum background. As mentioned previously and to summarize: the absolute signal efficiency is 1.7% in the fit region with an expected signal-to-background ratio of 0.03. The expected signal-to-background ratio in the signal region is 0.36.

In Table 6.4 the number of expected signal and background events after all selection cuts is given. The numbers are derived from Monte Carlo data. In the fit region 98.6 signal events are expected. From combinatoric signal one expects 36.7 events. For the background one notices that the $B \to X_c \ell \nu$ background with expected 2423.1 events is the largest background source. The second column gives the number of expected events for the signal region. The scaling factor f_{etalnu} (see Chapter 7) has been applied to the $B^+ \to \eta\ell^+\nu$ signal and $B^+ \to \eta\ell^+\nu$ combinatoric signal. The scaling factor f_{Xclnu} has been applied to the semileptonic $B \to X_c l\nu$.
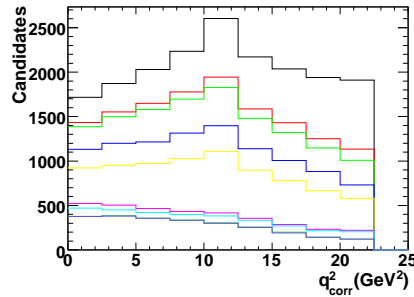
Figure 6.5: The q^2 spectrum after each cut. The black line shows the q^2 spectrum after the preselection cuts before all signal selection cuts. The red line shows the q^2 spectrum after the additional $m_{\gamma\gamma}^{\pi^0}$ (red), the green is M_h (green), $L2$ (blue), $cos\theta_{Thrust}$ (yellow), M_{miss}^2 (pink), θ_{miss} (light blue), p_{miss} (dark green), E_γ (violet) cut.

Efficiency Summary					
	$B^+ \to \eta \ell^+ \nu$ **Signal**		$B \to X_u \ell \nu$ **Background**	**Other** $BB(clnu, other, fake)$ **Background**	$q\bar{q}$ **Background**	**Total Background**
	Number of candidate after preselection					
Preselection $N_{candidates}$	1867.0		45890.9	278629.5	133726.9	458247.3
	single all-but-one selection cut eff.(%)					
$0.110 < m_{\gamma\gamma}^{\pi^0} < 0.160 GeV$	62.7		24.6	30.2	8.7	26.8
$0.50 < M_h < 0.58$ GeV	85.8		61.5	64.1	15.2	57.2
$L2 < 1.7$	91.2		77.6	68.9	13.1	60.8
$cos\theta_{Thrust} < 0.6$	89.0		88.1	86.8	16.0	75.2
$M_{miss}^2 < 3.0$	43.8		35.6	26.4	7.9	25.4
$0.7 < p_{miss} < 3.0$	81.4		78.1	85.5	18.3	74.6
$\theta_{miss} > 0.4$	94.6		95.6	89.9	19.2	80.2
$E_\gamma > 0.1 GeV$	97.1		94.5	93.3	19.2	82.2

Table 6.3: Efficiency table: number of candidates after preselection cuts and selection cut efficiencies. The later is in all-but-one mode, with $\epsilon_{\mathrm{all-but-one}} = \frac{N_{\mathrm{allcuts}}}{N_{\mathrm{allcutsbutone}}}$.

Number of expected data events		
	Fit Region	Signal Region
Data	3823	177
Total MC	3851.0	154.8
Signal (MC)	98.6	36.7
Combinatoric Signal (MC)	19.3	4.0
exclusive $B \to X_u \ell \nu$ (MC)	193.5	17.6
non-resonant $B \to X_u \ell \nu$ (MC)	380.9	22.5
$B \to X_c \ell \nu$ (MC)	2423.1	46.2
$B \to other$ (MC)	208.6	7.4
$q\bar{q}$ (MC)	527.0	20.4

Table 6.4: From Monte Carlo (MC) derived expected data events for each background source and the signal channel in the fit region and signal region. The scaling factor f_{etalnu} (see Chapter 7) has been applied to the $B \to \eta l \nu$ signal and $B \to \eta l \nu$ combinatoric signal. The scaling factor f_{Xclnu} has been applied to the semileptonic $B \to X_c l \nu$.

6.5 Data to Monte Carlo Comparison

In the following section three sets of data samples are compared with Monte Carlo data. These are the off-peak data in Section 6.5.1, an on-peak $B \to X_c \ell \nu$ enhanced data sample in Section 6.5.2, and the on-peak data for the final selection (all cuts applied) in Section 6.5.3.

6.5.1 Off-Peak Data to Continuum Monte Carlo Comparison

The off-peak data are used to study the agreement between data and continuum simulation. To achieve a statistically meaningful comparison of off-peak data with continuum Monte Carlo, the data-Monte Carlo agreement is studied using a sample with "relaxed continuum suppression", which corresponds to a selection with all cuts but the $L2$ and $cos\theta_{thrust}$ cut. This sample contains about ten times more continuum candidates than the final selection.

Figures 6.7 and 6.8 show a number of distributions for this sample in the signal region. In all these distributions, the continuum simulation has been scaled to the number of candidate in the off-peak data sample to allow a better comparison of the shapes (see Table 6.5 for the scaling factors). Since the composition of the continuum background differs for the electron and the muon channels, the distributions are shown for electrons and muons separately. For electrons, the continuum background consists mostly

of events with real electrons (shown as red histograms), while for muons the contribution from continuum events with a fake muon (shown as blue background) dominates. All variables show a reasonable data-Monte Carlo agreement for both electrons and muons within statistical precision of the off-peak data sample. This test indicates that the use of the continuum simulation in our analysis is a reasonable choice. The agreement for ΔE and m_{ES}, the two variables that are used to fit the signal contribution in this analysis, are shown in Fig. 6.9 for the signal band of the corresponding other variable. Figure 6.10 and Figure 6.11 show these two distributions for electrons and muons separately for the whole fit region for three different selection steps: the preselection, the relaxed continuum suppression, and final selection. Slight discrepancies are observed in ΔE and m_{ES} for the muon channel at the preselection level, but the overall agreement is still good.

The ratio of number of candidates in off-peak data and simulation is shown in Table 6.5 for the above mentioned three stages of the selection. These ratios, which can be used as normalization factors for the continuum simulation, are consistent for all three selection steps. For electrons, the factor lies above one, which could be an indication of an unsimulated continuum component that may be due to Bhabha or other QED processes. For muons, it is below one, which might be due to an imperfect understanding of the fake-lepton background.

Continuum MC normalization factor		
Selection	Electrons	Muons
Preselection	1.14 ± 0.02	0.89 ± 0.01
Relaxed continuum suppression	1.05 ± 0.07	0.86 ± 0.05
Final selection	1.01 ± 0.23	1.01 ± 0.18

Table 6.5: Scaling factors for continuum simulation derived from comparison with off-peak data for various steps of the selection.
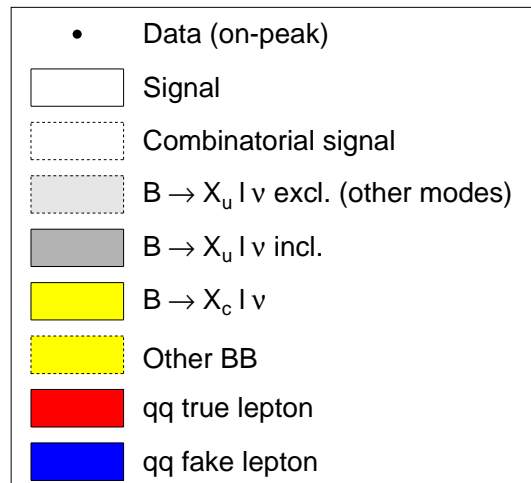
Figure 6.6: Legend for the following plots. The pink dashed line in the same of the plots illustrates the signal shape with an arbitrary normalization.

Relaxed Continuum Cuts, Signal Region

Electrons   **Muons**
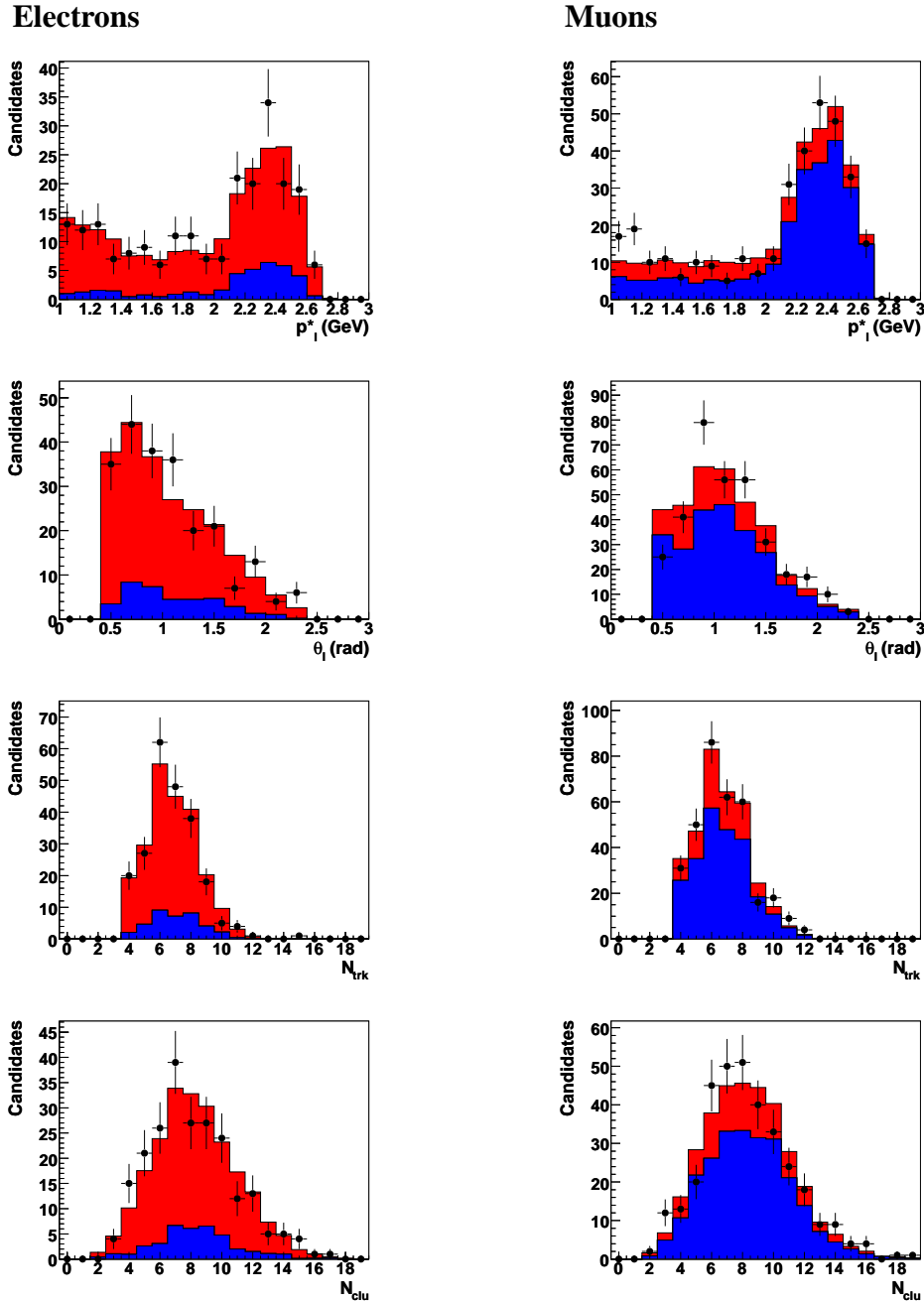
Figure 6.7: Simulated continuum background vs off-peak data. Off-peak data are shown as black circles with statistical errors. The histograms are simulated continuum events with true leptons (red) and fake leptons (blue). The continuum simulation has been scaled to the number of off-peak data candidates to facilitate a shape comparison (see Table 6.5 for the scaling factors). A legend can be found in Figure 6.6.

Relaxed Continuum Cuts, Signal Region

Electrons   **Muons**
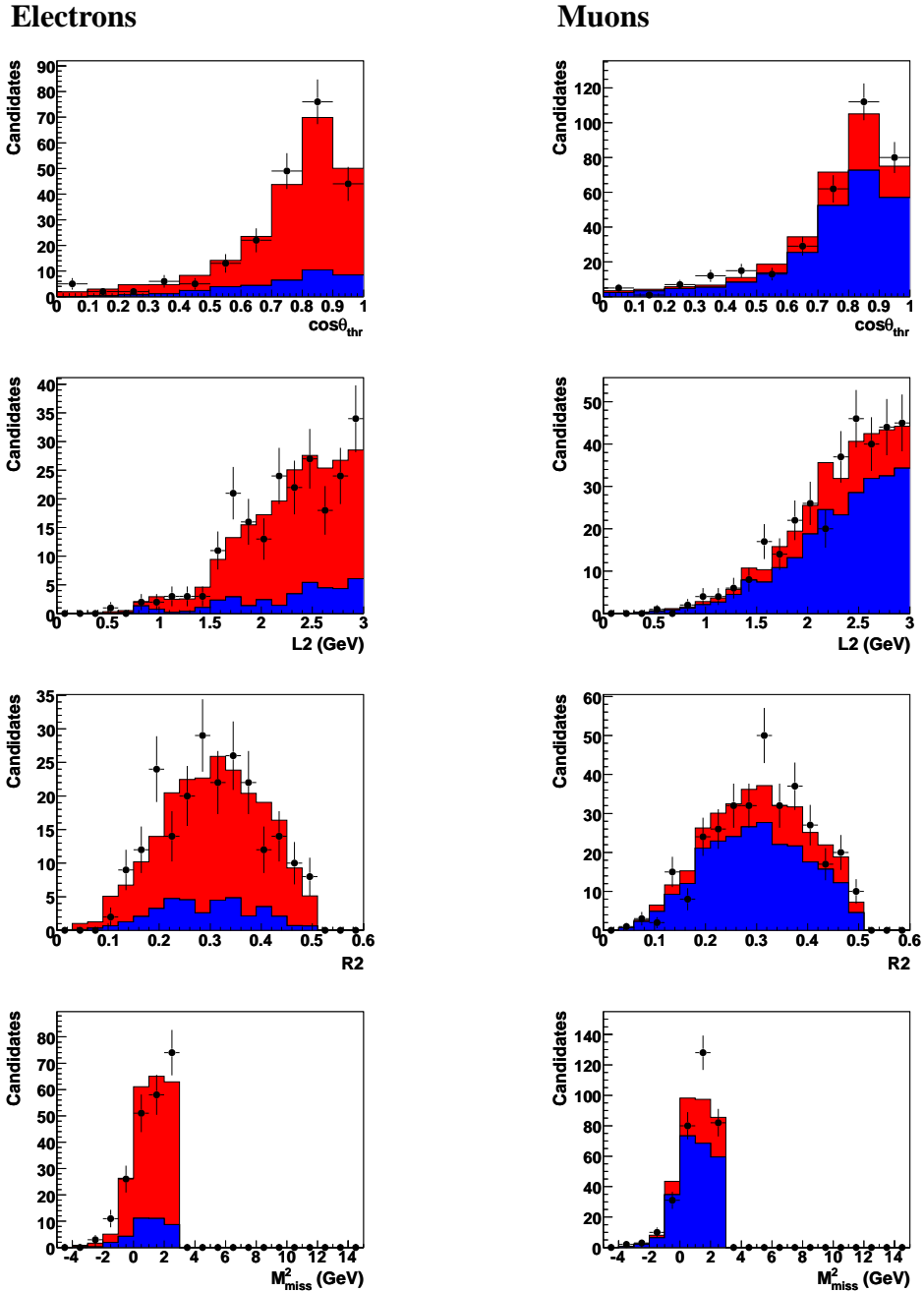
Figure 6.8: Simulated continuum background vs off-peak data. Off-peak data are shown as black circles with statistical errors. The histograms are simulated continuum events with true leptons (red) and fake leptons (blue). The continuum simulation has been scaled to the number of off-peak data candidates to facilitate a shape comparison (see Table 6.5 for the scaling factors). A legend can be found in Figure 6.6.

Relaxed Continuum Cuts: Top Row Side Band, Bottom Row Signal Band
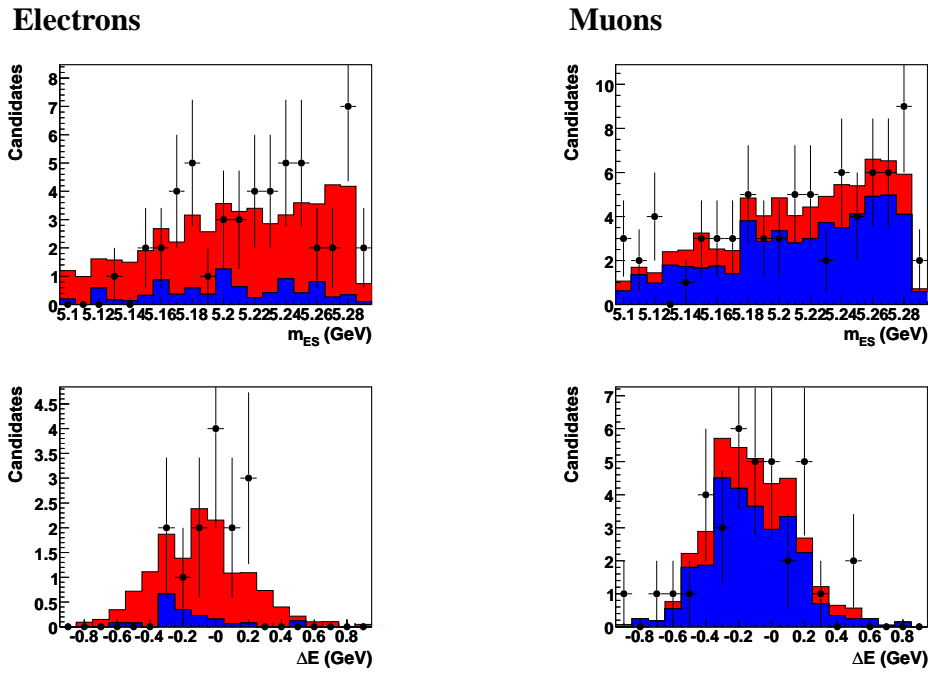
Figure 6.9: The q_{corr}^2, ΔE, and m_{ES} distributions: ΔE, and m_{ES} distributions are shown in the signal band of the m_{ES} and ΔE signal bands, respectively. Simulated continuum background vs off-peak data. Off-peak data are shown as black circles with statistical errors. The histograms are simulated continuum events with true leptons (red) and fake leptons (blue). The continuum simulation has been scaled to the number of off-peak data candidates to facilitate a shape comparison (see Table 6.5 for the scaling factors). A legend can be found in Figure 6.6.

Lepton = Electron

Preselection

Relaxed Continuum Suppression
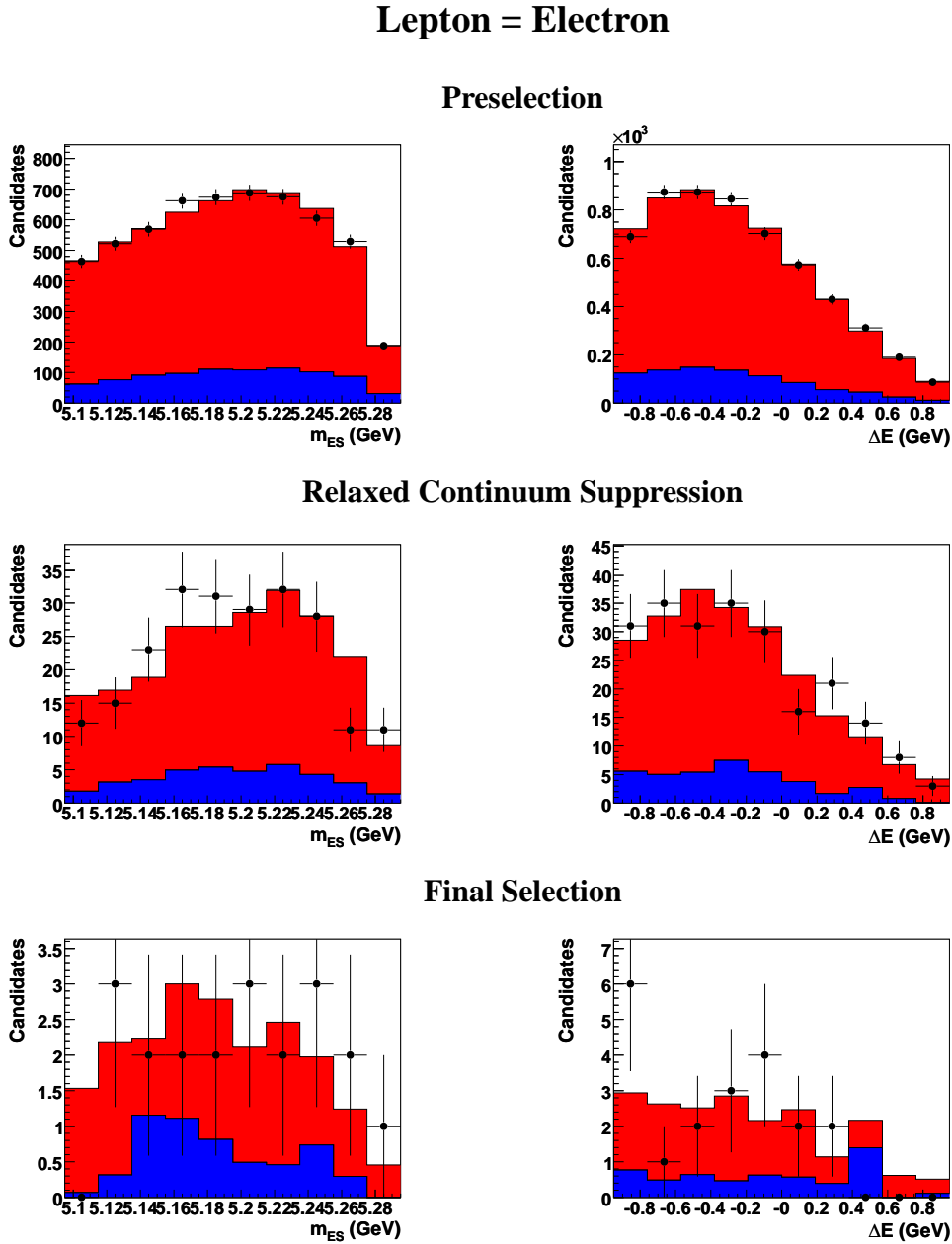
Final Selection

Figure 6.10: Comparison of m_{ES} (left) and ΔE (right) distributions for off-peak data and continuum simulation in the full ΔE vs. m_{ES} fit region. Three steps of the selection are shown: top = preselection, middle = all selection cuts except for the continuum suppression cuts on $L2$ and $\cos\theta_{thrust}$, bottom: all selection cuts. The continuum simulation has been scaled to the number of off-peak data candidates to facilitate a shape comparison (see Table 6.5 for the scaling factors). A legend can be found in Figure 6.6.

Lepton = Muon

Preselection
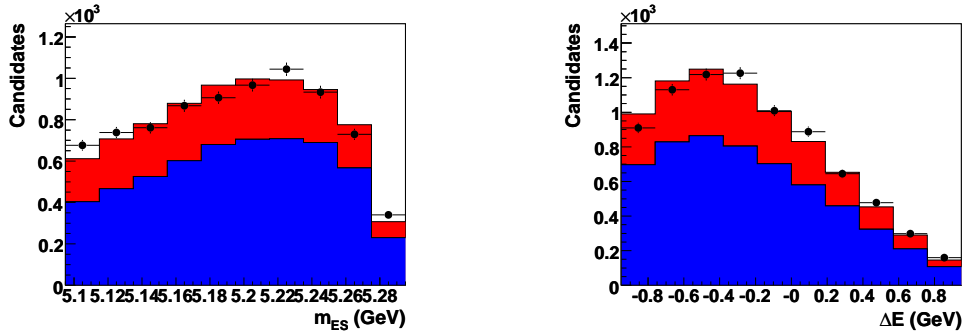
Relaxed Continuum Suppression
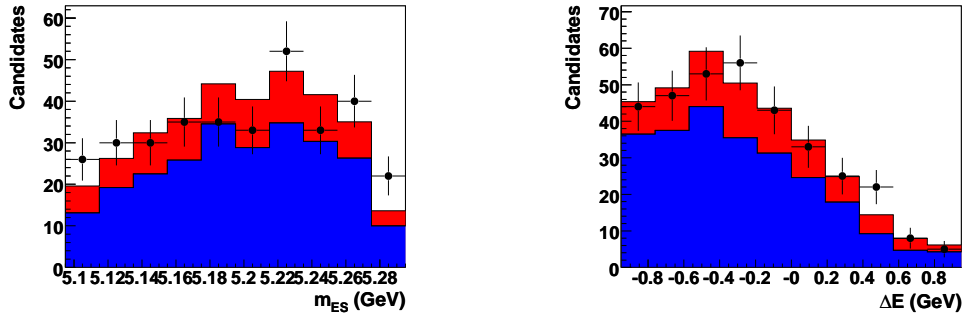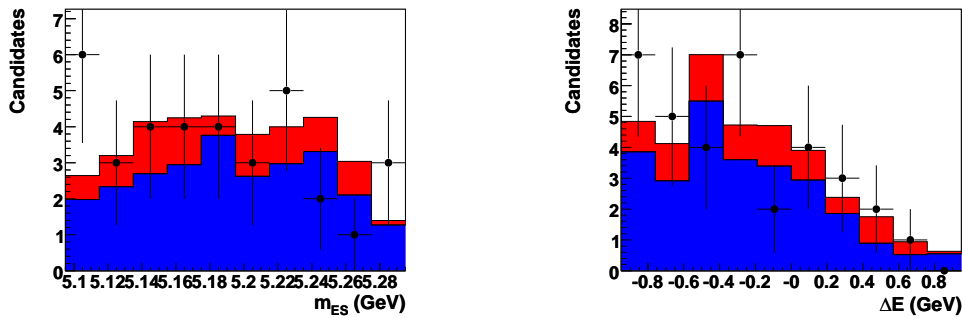
Final Selection

Figure 6.11: Comparison of m_{ES} (left) and ΔE (right) distributions for off-peak data and continuum simulation in the full ΔE vs. m_{ES} fit region. Three steps of the selection are shown: top = preselection, middle = all selection cuts except for the continuum suppression cuts on $L2$ and $\cos\theta_{thrust}$, bottom: all selection cuts. The continuum simulation has been scaled to the number of off-peak data candidates to facilitate a shape comparison (see Table 6.5 for the scaling factors). A legend can be found in Figure 6.6.

6.5.2 On-Peak Data to Monte Carlo Comparison for an $B \to X_c l \nu$ enhanced sample

To study the aggreement between $B \to X_c l \nu$ data and Monte Carlo a sample with "relaxed $B \to X_c l \nu$ suppression" is used, which corresponds to a selection with all cuts but the missing mass squared cut and the $m_{\gamma\gamma}^{\pi^0}$ veto cut. In Figure 6.12 a number of distributions for this sample is shown in the signal region. The data are below the Monte Carlo data for these cuts.

6.5.3 On-Peak Data to Monte Carlo Comparison for the Final Selection

Figure 6.13 to Figure 6.16 show distributions with the final selection cuts applied. It is important to notice that the Monte Carlo distribution have been scaled with the fit parameters from the fit (see Chapter 7). The agreement between the data distributions and the Monte Carlo distributions is good with only a minimal excess of data. All selection cuts have been applied except the one selection cut on the variable shown. The pink dashed line illustrates the signal shape with an arbitrary normalization.

Figure 6.13 shows the momenta in the center of mass system and polar angles for lepton, hadron and neutrino. Noticeable is that the hadron momenta distribution has a data overshoot at low hadron momenta. This could mean that the $B \to X_c \ell \nu$ or $B \to X_c \ell \nu$ sample which are the largest are not well described in this region. In Figure 6.14 the missing energy and mass are shown with $\cos\theta_{BY}$ and the three continuum background suppression variables $\cos\theta_{thr}$, $L2$, and $R2$. Only small deviation can be seen in the two variables describing the missing particle.

The following plot, Figure 6.15, shows in the top row two masses calculated from two photons, the $M_{\gamma\gamma}^{\pi0}$ veto and the η meson mass, which show good agreement. The η mass peak is clearly visible in the signal distribution as well as in the background distributions. The middle row shows the number of tracks and clusters in the events and in the bottom row one can find the corrected and uncorrected q^2 spectra. In Figure 6.16 the energies and the polar angles of the high and low energetic signal photons are shown.

In the next figure, Figure 6.17, one can find the ΔE distributions in the m_{ES} side band and the m_{ES} distribution in the ΔE side band (top row). The bottom row shows the same distributions in the signal band. For a definition of the signal and side band please see Chapter 5. Noticeable is that the ΔE distribution in the signal band has an unexplained data overshoot at zero.

Figure 6.3 and Figure 6.4 show the distributions for electrons and muons separately with only the preselection cuts applied. Figure 6.18 and Figure 6.19 show the distributions for electrons and muons separately with all cuts applied. The agreement is good.
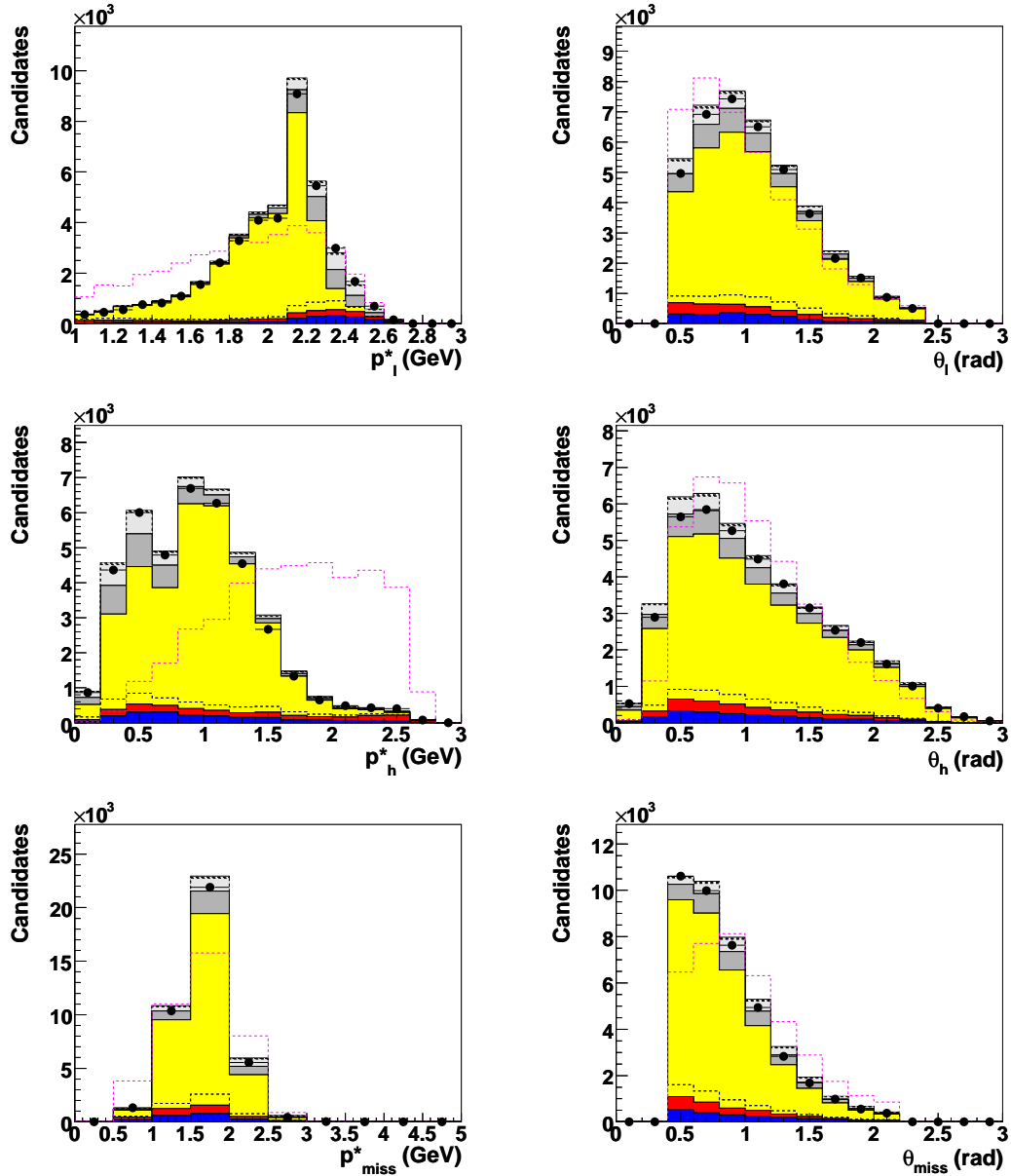
Figure 6.12: Enhanced $B \to X_c l \nu$ background sample versus on-peak data. All selection cuts have been applied except the cut on the missing mass and the $m_{\gamma\gamma}^{\pi^0}$ veto cut. The pink dashed line illustrates the signal shape with an arbitrary normalization. The position of the selection cuts are illustrated with a red line. A legend can be found in Figure 6.6.
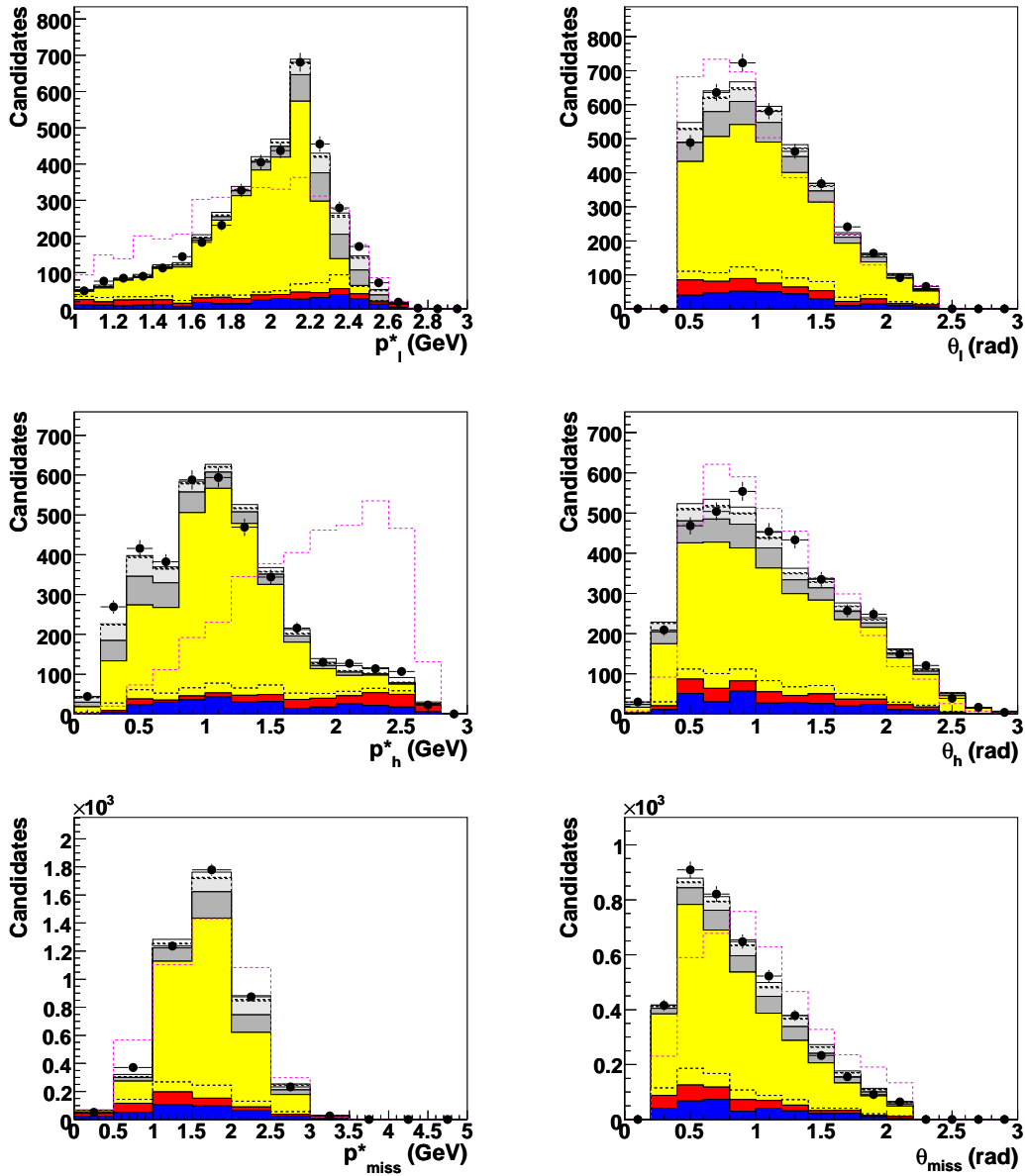
Final Selection

Figure 6.13: Momenta in the center of mass system and polar angles for lepton, hadron and neutrino are shown. Shown are on-peak data and Monte Carlo data. All selection cuts have been applied except the one selection cut on the variable shown. The pink dashed line illustrates the signal shape with an arbitrary normalization. A legend can be found in Figure 6.6.
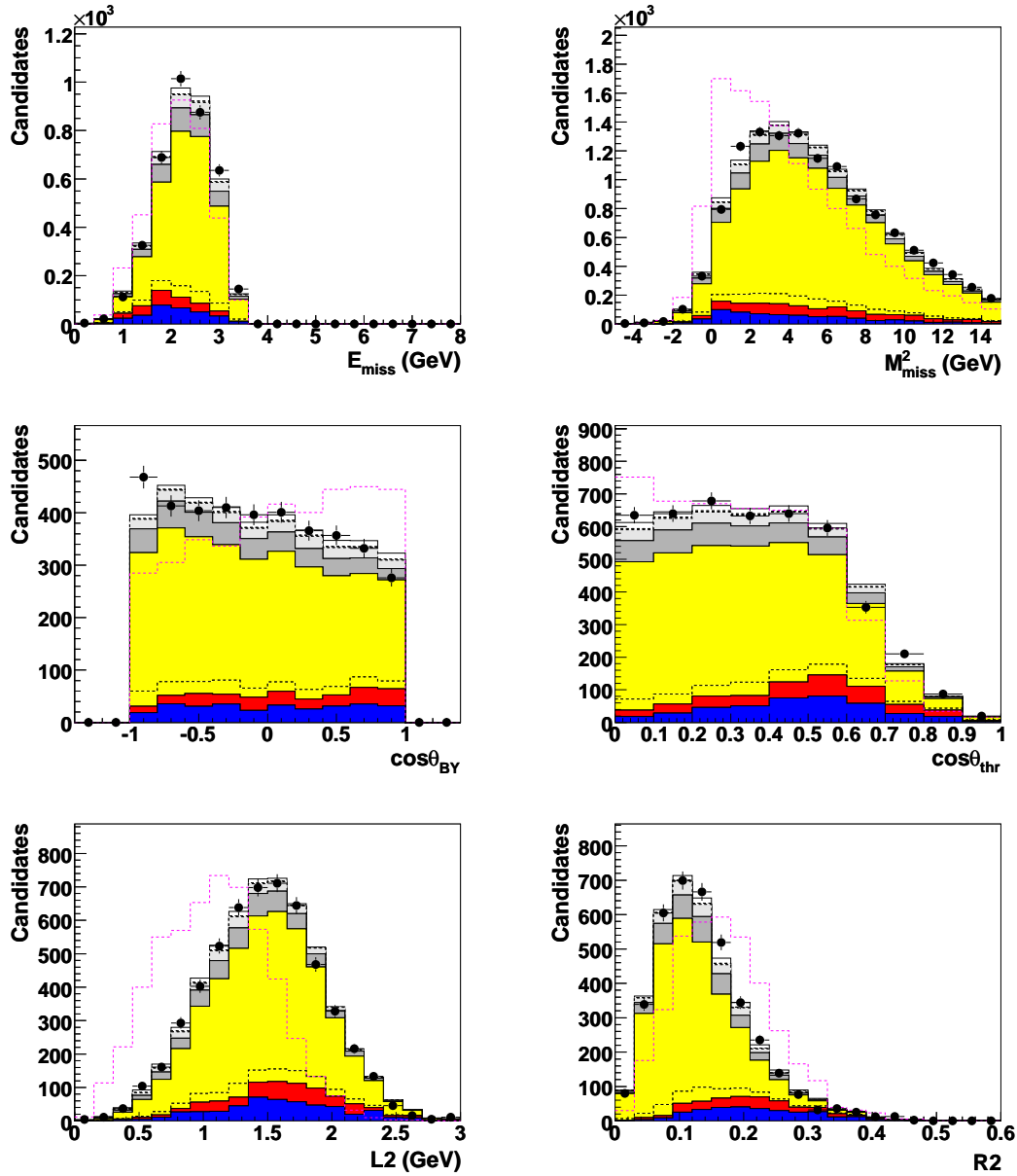
Final Selection

Figure 6.14: Neutrino quantities (E_{miss} and M_{miss}^2), $\cos\theta_{BY}$, and three continuum suppression variables, $\cos\theta_{thr}$, $L2$, and $R2$. Shown are on-peak data and Monte Carlo data. All selection cuts have been applied except the one selection cut on the variable shown. The pink dashed line illustrates the signal shape with an arbitrary normalization. A legend can be found in Figure 6.6.
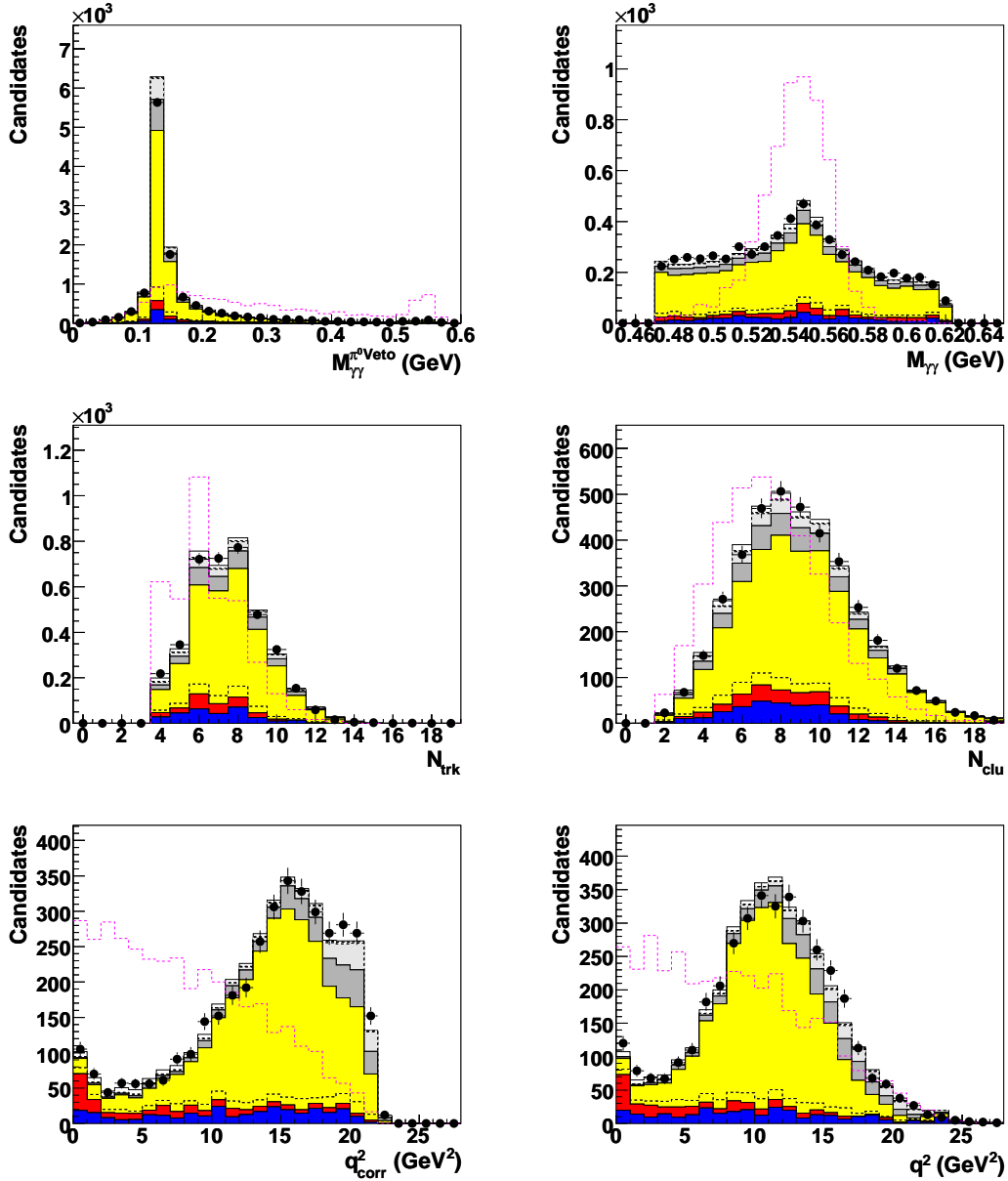
Figure 6.15: $M_{\gamma\gamma}^{\pi 0}$ veto and the η meson are shown in the top row, the number of tracks and clusters in the middle row and the corrected and uncorrected q^2 spectra in the bottom row. Shown are on-peak data and Monte Carlo data. All selection cuts have been applied except the one selection cut on the variable shown. The pink dashed line illustrates the signal shape with an arbitrary normalization. A legend can be found in Figure 6.6.
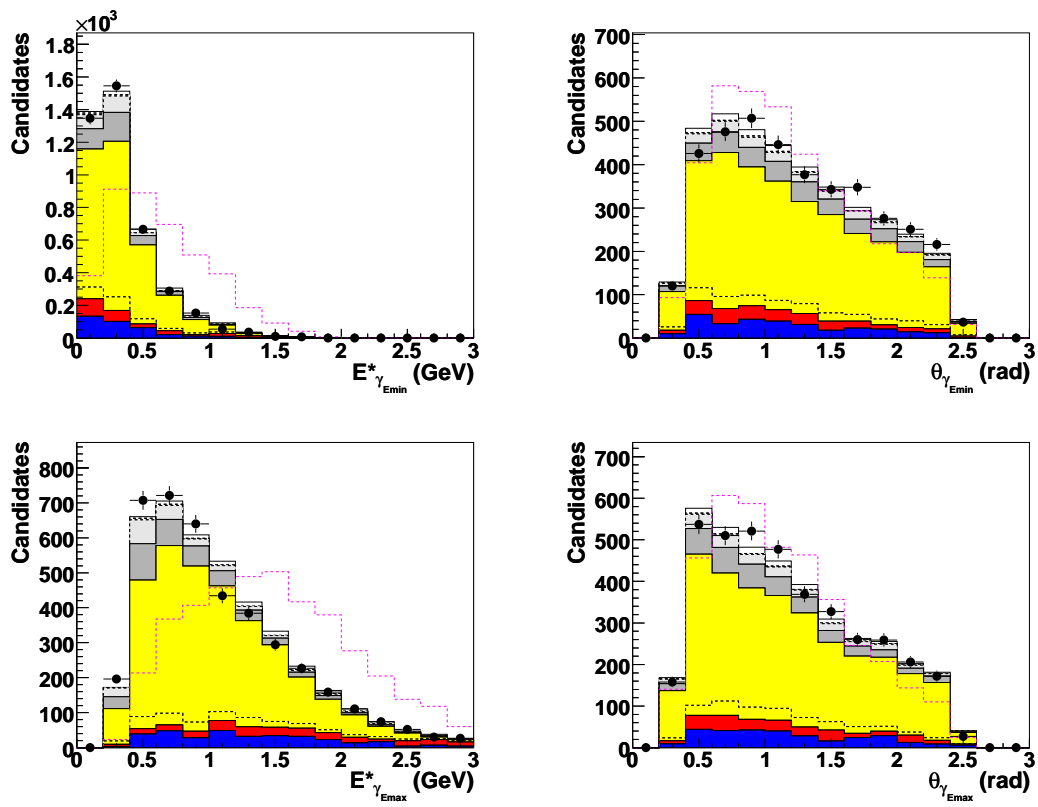
Final Selection

Figure 6.16: Energies and polar angle of the two signal photons. Shown are on-peak data and Monte Carlo data. All selection cuts have been applied except the one selection cut on the variable shown. The pink dashed line illustrates the signal shape with an arbitrary normalization. A legend can be found in Figure 6.6.

Final Selection: Top Row Side Band, Bottom Row Signal Band
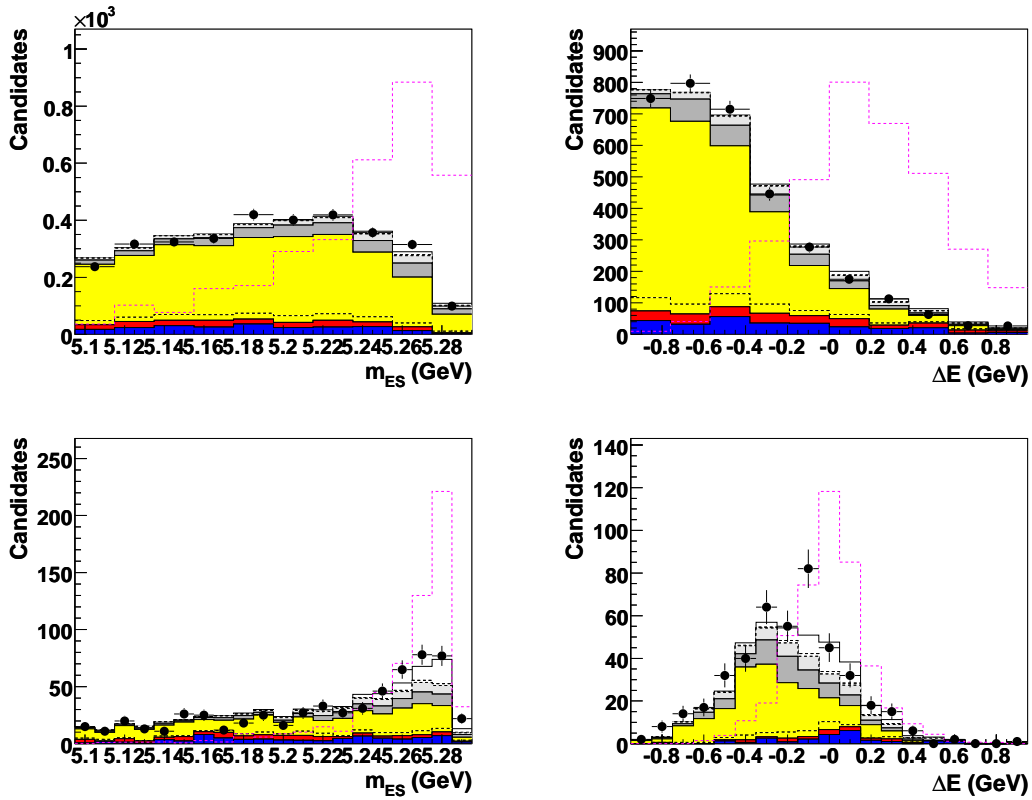
Figure 6.17: m_{ES} and ΔE distributions shown in the side band (top) and the signal band (bottom) (definition in Chapter 6). Shown are on-peak data and Monte Carlo data. All selection cuts have been applied except the one selection cut on the variable shown. The pink dashed line illustrates the signal shape with an arbitrary normalization. A legend can be found in Figure 6.6.

Final Selection for Electrons only
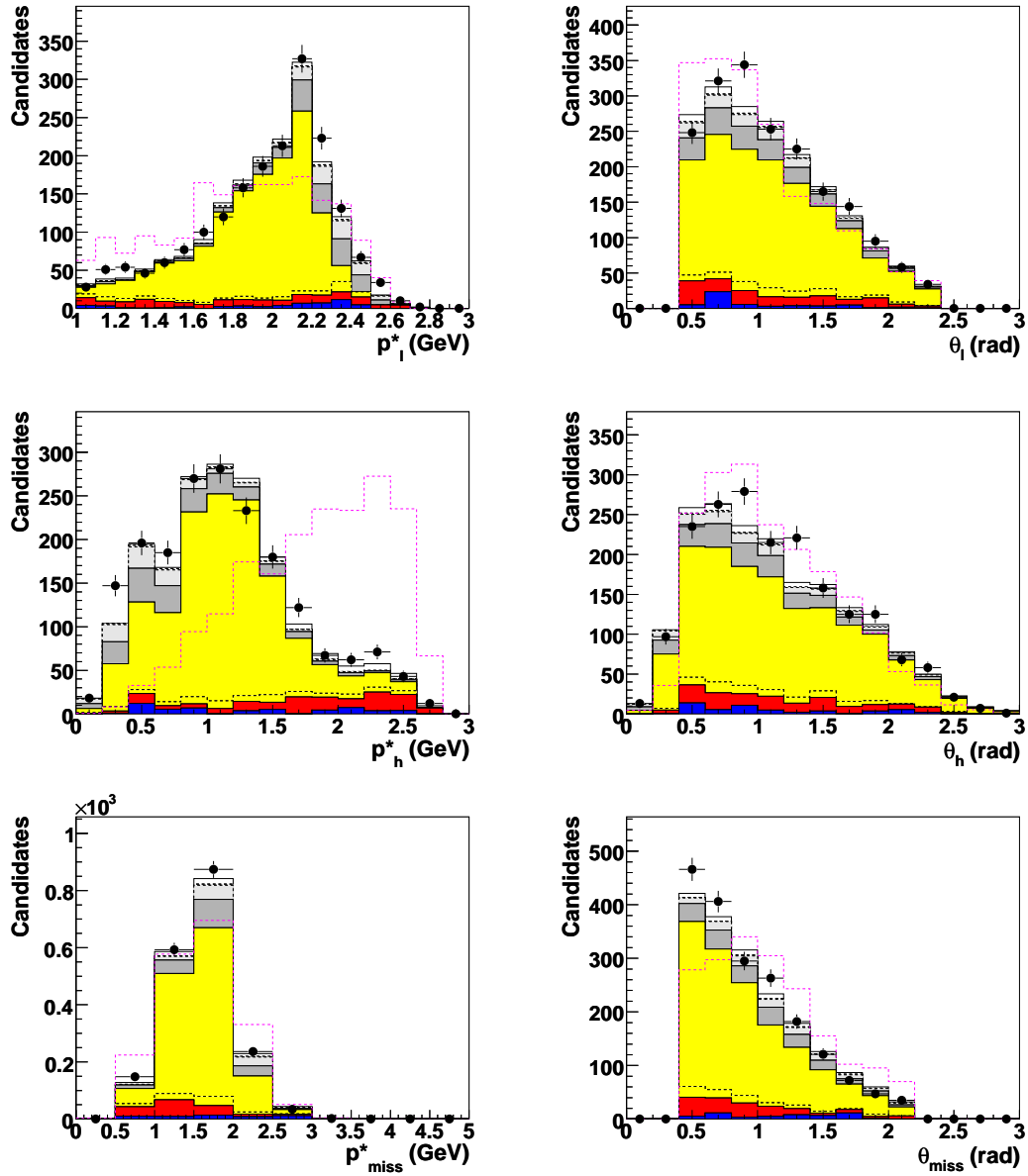
Figure 6.18: Momenta in the center of mass system and polar angles for lepton, hadron and neutrino are shown. Shown are on-peak data and Monte Carlo data for electrons only. All selection cuts have been applied except the one selection cut on the variable shown. The pink dashed line illustrates the signal shape with an arbitrary normalization. A legend can be found in Figure 6.6.
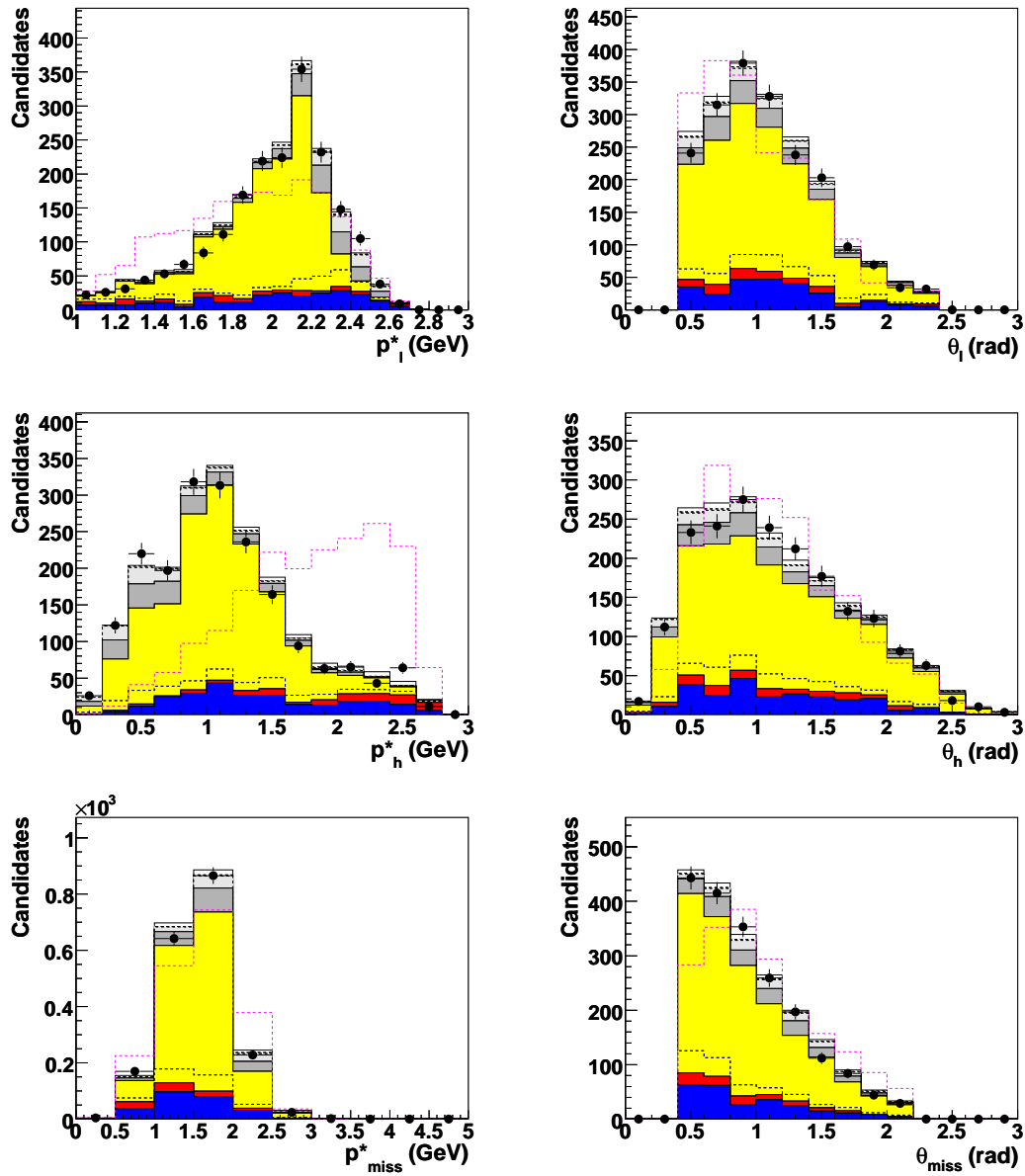
Figure 6.19: Momenta in the center of mass system and polar angles for lepton, hadron and neutrino are shown. Shown are on-peak data and Monte Carlo data for muons only. All selection cuts have been applied except the one selection cut on the variable shown. The pink dashed line illustrates the signal shape with an arbitrary normalization. A legend can be found in Figure 6.6.

Chapter 7

Extraction of the Branching Fraction

7.1 Fit Technique

To measure the branching fraction of $B^+ \to \eta(\to \gamma\gamma)l\nu$, a fit of the different Monte Carlo sources to the data distribution in two variables is performed. For the fit a 2-dimensional distribution of m_{ES} and ΔE is used. The region in the ΔE vs. m_{ES} plane in which the events must lie (fit region) was defined in Chapter 5:

$$|\Delta E| < 0.95 \; GeV \quad , \quad 5.095 < m_{ES} < 5.295 \; GeV \qquad (7.1)$$

An example plot of the 2-dimensional m_{ES} vs ΔE distribution of Monte Carlo signal events after all selection cuts have been applied is shown in Figure 7.1. To differentiate between the shapes of signal and background a very fine binning is used (Figure 7.1) in the region where the signal is located.

Another distribution that would be a candidate for the fit is the η mass $m_{\gamma\gamma}$ distribution. However the backgrounds also contain true η mesons and thus exhibit a peak at the reconstructed η mass. Also, the $m_{\gamma\gamma}$ variable does not provide a better discrimination of the various backgrounds than ΔE or m_{ES}, and thus does not allow an independent fit of these backgrounds either.

The fit method used is a generalized binned likelihood method which takes into account the statistical fluctuations not only of the data but also of the Monte Carlo sample. It was introduced by R. Barlow and C. Beeston. For a detailed discussion see the references [23] and [2]. Below a short summary is given.

The likelihood function $\mathcal{L}$ used in this analysis corresponds to the combined Poisson probability for the observed number of data events d_i and the number of accepted Monte Carlo events a_{ji}:

$$\ln\mathcal{L} = \sum_{i=1}^{n}(d_i \ln r_i - r_i) + \sum_{i=1}^{n}\sum_{j=1}^{m}(a_{ji} \ln A_{ji} - A_{ji}), \qquad (7.2)$$

where r_i is the sum of all fit contributions in bin i (see Equation 7.3). The A_{ji}'s are the estimated means of the Poisson distribution the a_{ji} were generated from, for bin i and
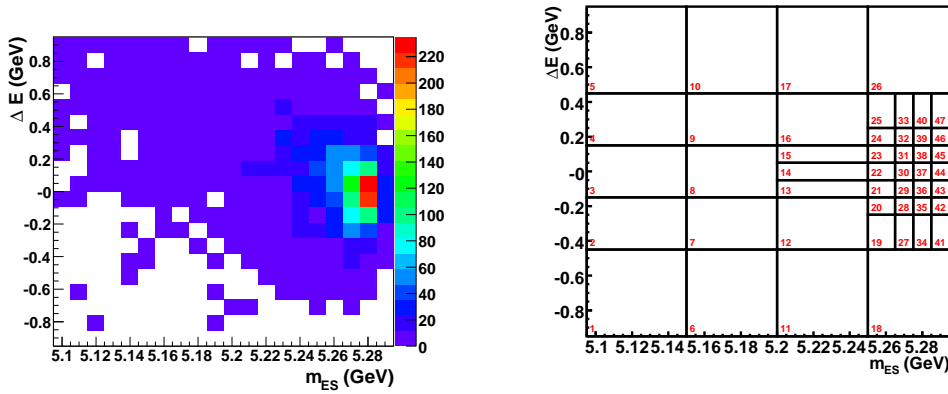
Figure 7.1: Left: ΔE vs. m_{ES} distribution for truth-matched signal after the all selection cuts. Right: Binning used in the fit.

for the background and signal samples j. The first term of Equation 7.2 accounts for the statistical fluctuations of the Monte Carlo samples, which is the difference between the Barlow-Beeston fit[1] and a standard maximum likelihood fit.

The sum of r_i of the fit contributions is given by

$$r_i = \sum_{j=1}^{m} f_j w_{ji} A_{ji},$$ (7.3)

where f_j is a parameter describing the relative normalization of the fit component j and w_{ji} is the weight for the events from the contributions j in bin i. There are different sources of weights, which are included in the w_{ij}:

- Global weight: the normalization to the number of $B\bar{B}$ events (for B decays), and to the integrated luminosity of on-peak data sample (for continuum events).

- Event weights: these are applied to each event individually. These weights include for instance

  weights for the particle identification,

  weights for the correction of the photon and K_L^0 efficiencies, and

  weights for the signal and background branching fraction and form factor corrections.

There are $m = 6$ fit contributions considered for the sum in Equation 7.3. For the fit to the data, this analysis however uses only two free parameter and the other parameters are fixed. Reason are given in Section 7.3. The possible fit contribution are:

---

[1]This fit uses the MINUIT package to maximize the likelihood function in Equation 7.2

$B^+ \rightarrow \eta\ell^+\nu(f_1 = f_{etalnu})$: Signal and combinatoric signal scale with the same branching fraction and the same fit parameter is used to measure the branching fraction.

$\mathrm{Resonant B} \rightarrow \mathrm{X_u}\ell\nu(\mathrm{f}_2 = \mathrm{f}_{\mathrm{Xulnu}}^{\mathrm{exclusive}})$: All other simulated exclusive semileptonic $B \rightarrow X_u\ell\nu$ decays ($X_u = \pi^-, \pi^0, \rho^0, \rho^-, \omega, \eta'$) are included here.

$\mathrm{Non-resonant B} \rightarrow \mathrm{X_u}\ell\nu(\mathrm{f}_3 = \mathrm{f}_{\mathrm{Xulnu}}^{\mathrm{inclusive}})$: The inclusive $B \rightarrow X_u\ell\nu$ for both B charges are combined.

$B \rightarrow X_c\ell\nu(f_4 = f_{Xclnu})$: Semileptonic $B \rightarrow X_c\ell\nu$ decays for both B charges are combined.

$\mathrm{Other B\bar{B}}(\mathrm{f}_5 = \mathrm{f}_{\mathrm{Bother}})$: All other simulated B decays ($B \rightarrow other$, $B\bar{B}$ with fake lepton) are combined.

$q\bar{q}(f_6 = f_{qq})$: Simulated $e^+e^- \rightarrow q\bar{q}$ with $q = u, d, s, c$ with fake and true leptons are combined.

7.2 Goodness of the Fit

The goodness of the maximum likelihood fit is evaluated by comparing the fitted Monte Carlo distribution with the data using a χ^2 approach: the χ^2 contribution of each bin of the m_{ES} vs ΔE distribution is calculated and summed over all bins:

$$\chi^2 = \sum_i^{N_{bins}} (N_i^{data} - N_i^{MC})^2/\sigma_i^{stat,data} \tag{7.4}$$

where N_i^{data} and N_i^{MC} are the numbers of entries in the i-th bin of the m_{ES} vs ΔE distribution and $\sigma_i^{stat,data}$ is the statistical error in the i-th data bin. The fit uses 47 bins and as mentioned above has two free fit parameters (f_{etalnu}, f_{Xclnu}) which reduces the number of degrees of freedom (ndf) to 45. Ideally the χ^2/ndf distribution should be one. The results from the χ^2 calculation as well as the probability of the χ^2 value are shown in the next chapter.

7.3 Toy Studies

Before a fit with real data is performed, extensive studies of fits of the Monte Carlo samples to toy data are done. In each bin of the the m_{ES} vs ΔE distribution a number of toy data is randomly produced using a Poisson probability function that uses the Monte Carlo value as mean. In this way a toy data distribution is generated for each signal and background sample. In these toy studies, the toy data are used instead of the real data and the probability density functions for the fit are still taken from the Monte Carlo distributions.

With these toy data correlations between the fit parameters (Section 7.3.1) and the fit reliability (Section 7.3.2) were studied on the basis of Monte Carlo data.

7.3.1   Correlation between the Fit Parameters

The fit automatically determines the correlations between the fit parameters f_x described in Section 7.1. The correlation matrices are taken from one example toy data fit. Different toy data fits with the same parameters have very similar correlation matrices and thus only one example is shown.

High correlations between fit parameters are not desired since an independent measurement of highly correlated sources is not possible and results of those fits can not be trusted. How many background parameters are fitted is a trade-off between the fit stability and the systematic error: if the shape of two distributions is similar the correlation is high and the fit can become unstable. Studies with two to six free fit parameters f_x in various combinations were done. Results of some of these studies using fits with two, three, or four free fit parameters are shown below:

4 free parameters (f_{qq}, f_{Xclnu}, $f_{Xulnu}^{inclusive}$, f_{etalnu})**:**

Fitting the parameter f_{qq}, f_{Xclnu}, $f_{Xulnu}^{inclusive}$, and f_{etalnu} and leaving all others fit parameters fixed to 1.0 yields a large correlation of almost 80% between f_{Xclnu} and $f_{Xulnu}^{inclusive}$ due to their similar shape. Since also signal is highly correlated it has a direct effect on the result of f_{etalnu} and thus one needs to be excluded. f_{Xclnu} is kept since it is the largest background contribution. The correlation matrix can be seen in Table 7.1.

Correlation Matrix				
	f_{qq}	f_{Xclnu}	$f_{Xulnu}^{inclusive}$	f_{etalnu}
f_{qq}	1.00	0.35	0.13	0.30
f_{Xclnu}	0.35	1.00	0.79	0.61
$f_{Xulnu}^{inclusive}$	0.13	0.79	1.00	0.65
f_{etalnu}	0.30	0.61	0.65	1.00

Table 7.1: Correlations between fit parameter f_{qq}, f_{Xclnu}, $f_{Xulnu}^{inclusive}$, and f_{etalnu}.

3 free parameters (f_{qq}, f_{Xclnu}, f_{etalnu})**:**

Fitting f_{qq}, f_{Xclnu}, and f_{etalnu} and leaving all others fit parameters fixed to 1.0 results in high correlation between f_{qq} and f_{Xclnu} (73%). The signal fit parameter is also highly correlated with the f_{qq} (50%). f_{qq} is fixed since the continuum background has lower statistics than the semileptonic $B \rightarrow X_c \ell \nu$ background (f_{Xclnu}). The correlation matrix can be seen in Table 7.2.

2 free parameters (f_{Xclnu}, f_{etalnu})**:**

Correlation Matrix			
	f_{qq}	f_{Xclnu}	f_{etalnu}
f_{qq}	1.00	0.73	0.50
f_{Xclnu}	0.73	1.00	0.20
f_{etalnu}	0.50	0.20	1.00

Table 7.2: Correlations between fit parameter f_{qq}, f_{Xclnu}, and f_{etalnu}.

The version used in this analysis fits two parameters: The signal parameter, f_{etalnu}, and the background fit parameter, f_{Xclnu}. All all others fit parameters were fixed to 1.0. The correlation between $B^+ \rightarrow \eta \ell^+ \nu$ and semileptonic $B \rightarrow X_c \ell \nu$ background decays in this fit are 27% and this fit with low correlations can now be trusted to give us a reliable result for the measurement of the branching fraction. The correlation matrix can be seen in Table 7.3.

Correlation Matrix		
	f_{X_c}	f_{eta}
f_{X_c}	1.00	-0.26
f_{eta}	-0.26	1.00

Table 7.3: Correlations between fit parameter f_{etalnu} and f_{Xclnu}

7.3.2   Fit Validation

In order to study the validity of the fit, the Monte Carlo samples were fitted to 1000 different toy data distributions. For each of these 1000 fits, a value for $(N_{fit} - N_{true}/\sigma)$ is computed where N_{fit} is the number of toy data events after the fit and N_{true} is the number of toy data events before the fit and σ refers to the error. With these values one can plot so-called "pull" distributions which are shown in Figure 7.2. Ideally a Gaussian curve is expected. If the mean (μ) of this Gaussian is not zero a bias in present, if the width (σ) is not one the errors are overestimates ($\sigma < 1$) or underestimated ($\sigma > 1$). From a fit of a Gaussian function to the "pull" distribution the mean and the width are obtained and shown in the plots. No bias is seen in the distributions and only a small overestimation of the errors in the $B \rightarrow X_c \ell \nu$ background channel is present. The mean and the width for the signal fit parameter look good.
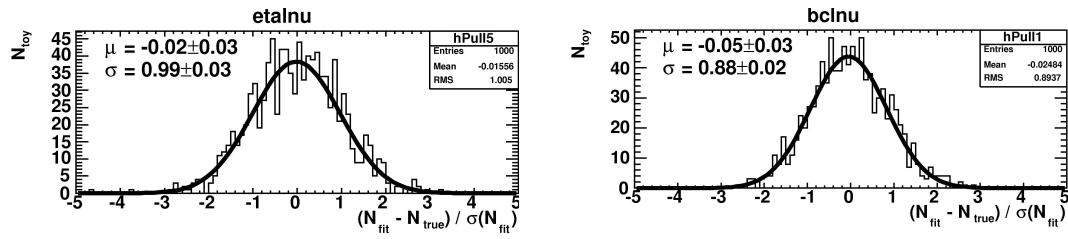
Figure 7.2: "Pull" distributions obtained with 1000 toy generations. The toys were generated randomly from the simulated samples using a Poisson distribution.

Chapter 8

Results with Data

8.1 Fit Results

As mentioned in the previous chapter the fit to the data yields the two scaling factors for $B \to \eta(\to \gamma\gamma)\ell\nu$ (f_{etalnu}) and the semileptonic $B \to X_c\ell\nu$ decays (f_{Xclnu}). The fit parameters can be translated into branching fractions as described in Section 8.3. The resulting fit parameters are shown in Table 8.1. f_{etalnu} scales the signal yield expected from the generated sample significantly down, $f_{etalnu} = 0.405\% \pm 0.111\%$, whereas the semileptonic $B \to X_c\ell\nu$ background are scaled up, $f_{Xclnu} = 1.097\% \pm 0.03\%$ relative to the simulation.

The large deviation from 1.0 of f_{Xclnu} is unexpected. One possible explanation is that due to the correlation between the background samples the not well described data to Monte Carlo agreement of the other background sample are balanced out by the fit with the $B \to X_c\ell\nu$ background. Some studies have been done to understand the 10% deviation. These are shown in the next chapters.

The goodness of fit evaluated with a χ^2 method described in the last chapter is 1.26 and the χ^2 probability is 12%.

Fit Result	
Parameter	
$B^+ \to \eta\ell^+\nu$, f_{etalnu}	0.405 ± 0.111
$B \to X_c\ell\nu$, f_{Xclnu}	1.097 ± 0.033
χ^2/ndf	$56.5/45 = 1.26$
Probability (%)	11.6

Table 8.1: Fit parameters for the $B \to \eta l\nu$ and $B \to X_c l\nu$ sample and the χ^2/ndf and probability for the fit to the data.

8.2   Fitted Distributions in Signal Region

In the following distributions the scaling factor f_{etalnu} has been applied to the $B \rightarrow \eta l\nu$ signal and $B \rightarrow \eta l\nu$ combinatoric signal and the semileptonic $B \rightarrow X_c\ell\nu$ sample has been scaled with the fit parameter f_{Xclnu}. The distributions are shown for the signal region (see Section 5.6 for definition) where the signal over background ratio is good. A legend can be found in Figure 8.1. In Table 8.2 a summary of the number of expected events is given after the scaling factors have been applied. The number of expected signal events is 98.7 ± 27.1 of which 36.7 ± 10.1 events are located in the signal region. The quoted error is the error from the fit.

Number of expected data events		
	Fit Region	Signal Region
Data	3823	177
Total MC	3851.0	154.8
Signal (MC)	98.7 ± 27.1	36.7 ± 10.1
Combinatoric Signal(MC)	19.3 ± 5.3	4.0 ± 1.1
$B \rightarrow X_c\ell\nu$ (MC)	2423.1 ± 72.9	46.2 ± 1.4
Other Background combined (MC)	1310.0	67.9

Table 8.2: From Monte Carlo derived expected data events for each background source and the signal channel in the fit region and signal region. The scaling factor f_{etalnu} has been applied to the $B \rightarrow \eta l\nu$ signal and $B \rightarrow \eta l\nu$ combinatoric signal. The scaling factor f_{Xclnu} has been applied to the semileptonic $B \rightarrow X_c l\nu$. All other Monte Carlo samples are combined and individual values can be found in Table 6.4 in Section 6.3.3.

The top row of Figure 8.2 shows the ΔE distribution in the m_{ES} side band and the m_{ES} distribution in the ΔE side band. The bottom row shows the same distributions in the signal band. The agreement in the side bands is good but there are too many data candidates compared to the Monte Carlo in the signal band. The following distributions are shown with all selection cuts applied and all show to many data events compared to the Monte Carlo sample. In Figure 8.3 the left column shows the center of mass momenta of the lepton, the neutrino, and the hadron. In the right column the polar angles of these variables are shown. Figure 8.4 shows the q_{corr}^2 spectrum, the energies and polar angles of the low and high energetic photon, and the reconstructed mass of the η meson. The mass distribution shows a peak at the η mass.
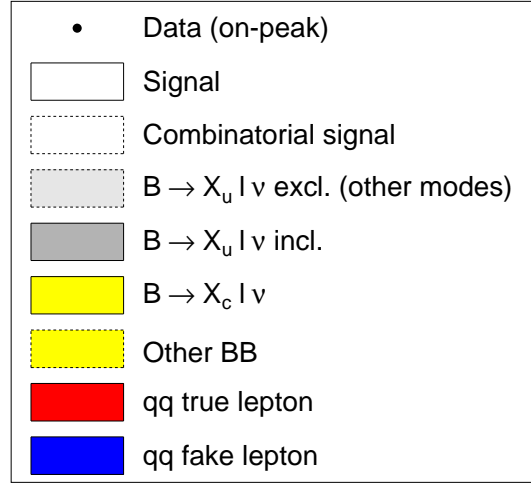
Figure 8.1: Legend for the following plots.

8.3 Branching Fraction Measurement

The fit parameter f_{etalnu} can be translated into a branching fraction for $B \rightarrow \eta(\rightarrow \gamma\gamma)\ell\nu$ by multiplying the scaling factor f_{etalnu} with the branching fraction ($\mathcal{B}(B^+ \rightarrow \eta\ell^+\nu)$) used in the Monte Carlo and the branching fraction of the $\eta \rightarrow \gamma\gamma$ decay ($\Gamma^{MC}_{\eta\rightarrow\gamma\gamma}/\Gamma^{MC}$):

$$\mathcal{B}(B^+ \rightarrow \eta(\rightarrow \gamma\gamma)\ell^+\nu) = \mathcal{B}(B^+ \rightarrow \eta\ell^+\nu) \cdot (\Gamma^{MC}_{\eta\rightarrow\gamma\gamma}/\Gamma^{MC}) \cdot f_{etalnu} \qquad (8.1)$$

$$\mathcal{B}(B^+ \rightarrow \eta(\rightarrow \gamma\gamma)\ell^+\nu) = (1.28 \pm 0.35) \cdot 10^{-5} \qquad (8.2)$$

where the shown error is the statistical error from the fit which includes the the error on the normalization of the semileptonic $B \rightarrow X_c\ell\nu$ background.

By using the well known $\eta \rightarrow \gamma\gamma$ decay rate one can translate the branching fraction of Equation 8.2 to a total branching fraction of $B^+ \rightarrow \eta\ell^+\nu$:

$$\mathcal{B}(B^+ \rightarrow \eta\ell^+\nu) = \mathcal{B}(B^+ \rightarrow \eta(\rightarrow \gamma\gamma)\ell^+\nu) \cdot (\Gamma^{PDG}/\Gamma_{\eta\rightarrow\gamma\gamma}) \qquad (8.3)$$

$$\mathcal{B}(B^+ \rightarrow \eta\ell^+\nu) = (3.25 \pm 0.89 \pm 0.02) \cdot 10^{-5} \qquad (8.4)$$

where the first error is the statistical error from the fit and the second error is due to the uncertainty on the PDG value for the $\eta \rightarrow \gamma\gamma$ decay rate ($\Gamma_{\eta\rightarrow\gamma\gamma}/\Gamma) = (39.38\pm0.26\%$, [15]).

The branching fraction of $B^+ \rightarrow \eta(\rightarrow \gamma\gamma)\ell^+\nu$ is measured with an statistical uncertainty of 27%, neglecting the systematic uncertainty. The systematic uncertainty are evaluated in Section 9.

8.4 Stability Tests

Test of the stability of the fit are done by:
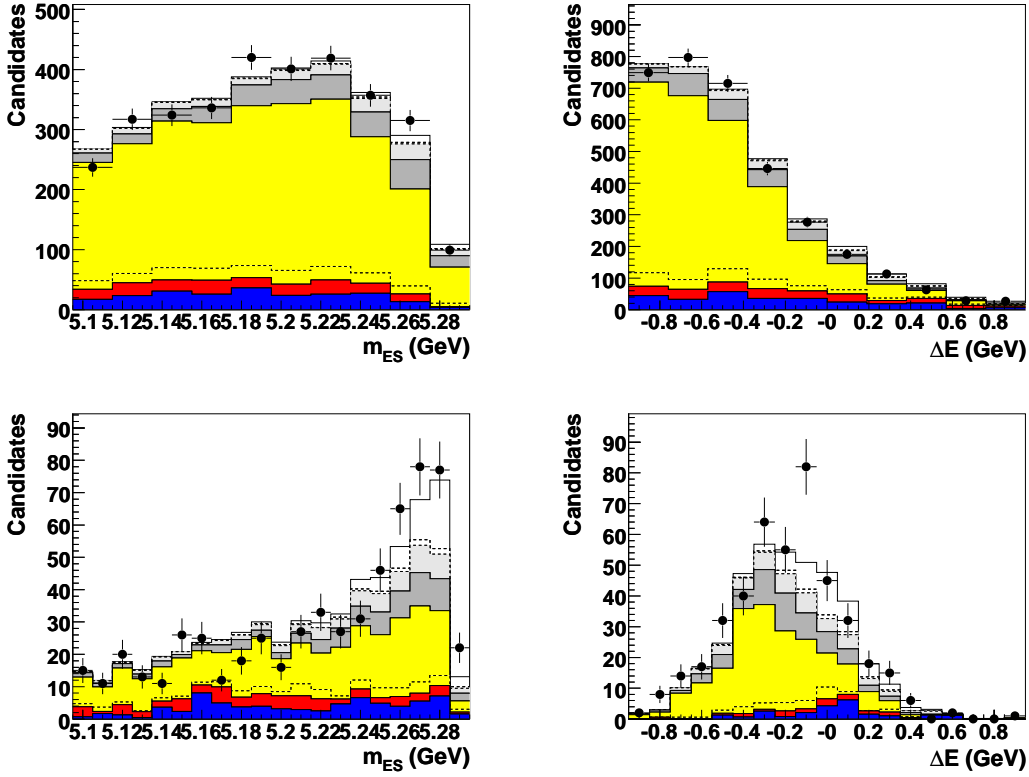
Figure 8.2: m_{ES} and ΔE shown in the side band and signal band (definition in 6) after all selection cuts. The signal and semileptonic $B \rightarrow X_c \ell \nu$ distributions have been scaled with the fit parameters f_{etalnu} and f_{Xclnu} respectively. A legend can be found in Figure 8.1.

1. Comparing Run1-Run3 data with Run4 data. Both samples have about the same data volume.

2. Splitting the data sample in decays with an electron and decays with a muon.

3. Varying three selection cuts: M^2_{miss}, $m^{\pi^0}_{\gamma\gamma}$, and M_h.

The result obtained for each of these tests are summarized in Table 8.3. The results for Run1-Run3 and Run4 are stable but the the difference between the nominal branching fraction and the branching fraction obtained for the electrons and muons sample are large. Especially the muon sample deviates from the nominal result. Further studies have to be performed to analyse why the discrepancies are so high.

For the missing mass cut variation one finds that the branching fraction decreases the weaker the cut becomes. This could result from the shift in the data to Monte Carlo distribution. Changing the $m^{\pi^0}_{\gamma\gamma}$ cut leaves the branching fraction stable with the exception of the very tight cut around the π^0 mass. The variation in the hadron

mass also leaves the branching fraction rather stable and only with very tigh cuts 20% differences are seen.
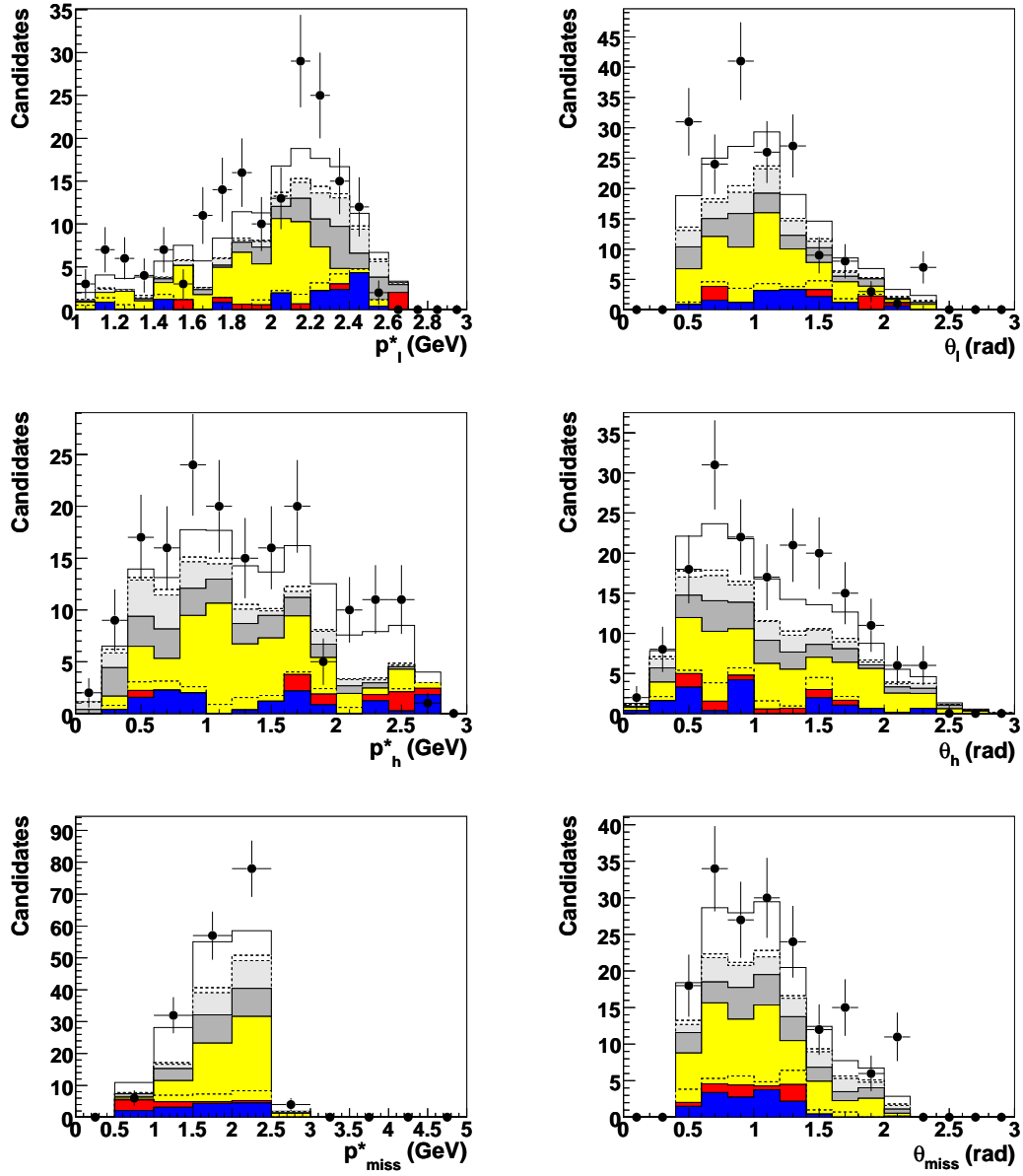
Figure 8.3: Momenta in the center of mass frame and polar angles for lepton, hadron and neutrino shown after all selection cuts. The signal and semileptonic $B \rightarrow X_c \ell \nu$ distributions have been scaled with the fit parameters f_{etalnu} and f_{Xclnu}, respectively. A legend can be found in Figure 8.1.
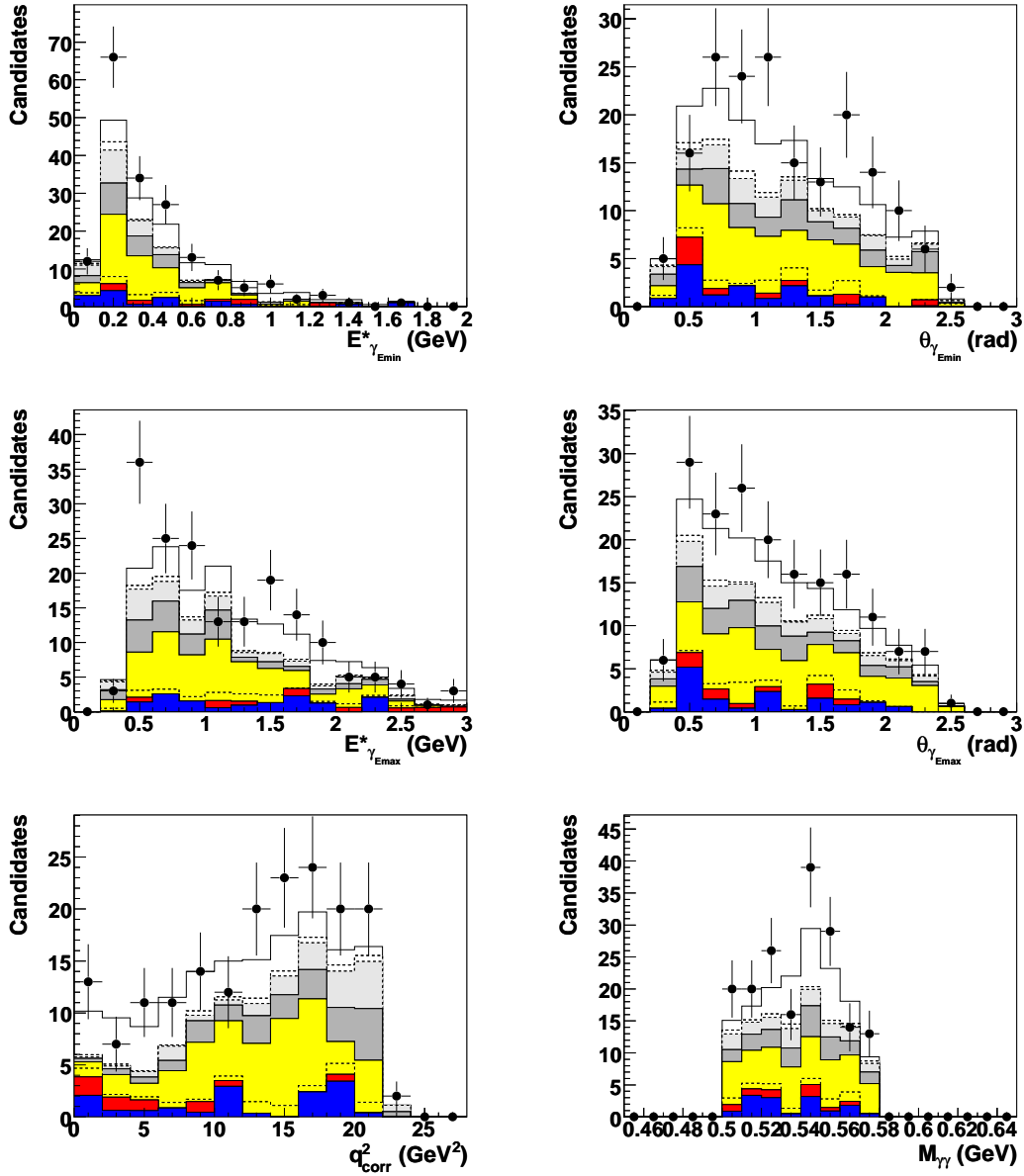
Figure 8.4: Momenta of the low and high energetic signal photons and their polar angle. The mass of the η and the q^2_{corr} spectrum (definition in 6) are shown in the bottom row. All variables are shown after all selection cuts. The signal and semileptonic $B \to X_c \ell \nu$ distributions have been scaled with the fit parameters f_{etalnu} and f_{Xclnu}, respectively. A legend can be found in Figure 8.1.

Data Set	BF of $B \rightarrow \eta(\rightarrow \gamma\gamma)\ell\nu(10^{-5})$	Difference in %
Nominal Result	1.28±0.35	-
Only Run1-3	1.58 ±0.48	23.4
Only Run4	1.24 ±0.66	3.1
Only Electron	1.82 ±0.50	42.2
Only Muons	0.51 ±0.45	60.2
Missing Mass Cut		
$M^2_{miss} < 2.0$ GeV^2	1.44± 0.38	12.5
$M^2_{miss} < 2.5$ GeV^2	1.39± 0.37	8.6
Nominal Cut: $M^2_{miss} < 3.0$ GeV^2	1.28±0.35	-
$M^2_{miss} < 3.5$ GeV^2	1.17± 0.39	8.9
$M^2_{miss} < 4.0$ GeV^2	0.92± 0.30	28.9
π^0 Veto Cut		
$0.130 < m^{\pi^0}_{\gamma\gamma} < 0.140 GeV$	0.88±0.33	30.1
$0.120 < m^{\pi^0}_{\gamma\gamma} < 0.150 GeV$	1.26±0.35	1.6
Nominal Cut: $0.110 < m^{\pi^0}_{\gamma\gamma} < 0.160 GeV$	1.28±0.35	-
$0.100 < m^{\pi^0}_{\gamma\gamma} < 0.170 GeV$	1.20±0.36	6.3
$0.090 < m^{\pi^0}_{\gamma\gamma} < 0.180 GeV$	1.33±0.36	3.9
Hadron Mass Cut		
$0.48 < M_h < 0.60 GeV$	1.31± 0.37	2.3
$0.49 < M_h < 0.59 GeV$	1.35± 0.35	5.5
Nominal Cut: $0.50 < M_h < 0.58 GeV$	1.28±0.35	-
$0.51 < M_h < 0.57 GeV$	1.03± 0.34	19.5
$0.52 < M_h < 0.56 GeV$	1.07± 0.35	16.4

Table 8.3: Difference of the branching fractions between the nominal result (Run1-4, electrons and muons included, and the nominal selection cuts) and the result obtained with only Run 1-3, Run 4, electrons, or muons and chages in important cuts.

Chapter 9

Systematic Uncertainties

9.1 Method

Data to Monte Carlo discrepancies originate from uncertainties of parameters which are taken from other analyses and are used in this analysis. These parameters can be for example branching fractions or form factors of B meson decays or reconstruction effects. To quantify the effect of these uncertainties on this analysis, an systematic error analysis is done.

Since this analysis reconstructs a neutrino contributions to the total rate of undetectable neutral particles must be accounted for. Contributions come from uncertainties in the charged and neutral particle reconstruction efficiency, beam background from tracks and photons, fake tracks and unmatched neutral clusters which occur when a charged track is not correctly matched to its cluster, and hadronic split offs all contribute. Also other particles which do not or only partly interact with the detector material such as other neutrinos, K_L^0's and neutrons contribute as well.

The systematic errors are divided into three categories.

Detector Effects which deals with how well the decay is reconstructed,

Physics Modeling which deals with how well the signal and background form factors and branching fractions are known, and

Other Systematic Uncertainties such as how well the number of produced B mesons, the $B^0 B^\pm$ lifetimes and fractions are known

The branching fraction obtained for $B^+ \to \eta(\to \gamma\gamma)\ell^+\nu$ is taken as the nominal value ($BF_{nominal}$). For the systematic error calculations the input quantity in question is changed within its uncertainty and the analysis is repeated. The difference between the nominal branching fraction and the branching fraction obtained with the changes (BF_{sys}) over the nominal value is taken as the systematic error on the quantity:

$$\sigma_{sys} = \frac{BF_{nominal} - BF_{sys.}}{BF_{nominal}}. \tag{9.1}$$

Each systematic uncertainty is assumed to be independent from one another and thus the total systematic error is obtained by adding the square of each individual systematic error.

The systematic errors of this analysis uses the analysis software of the $B \to \pi\ell\nu$ and $B \to \rho\ell\nu$ analysis. A detailed description of how the errors are calculated can be found in Reference [2]. Below a short description of the error and the value of each error is given.

9.2   Detector Effects

9.2.1   Track and Photon Efficiencies

The same reconstruction algorithm is used for data as well as simulated data (Monte Carlo). Reconstruction can differ for data and Monte Carlo. A "killing" is implemented as a random elimination of surplus tracks and photons with a certain probability. The probability corresponds to the difference in the number of data events and Monte Carlo events and is effected with an uncertainty.

The errors for track and photon uncertainties are given in Table 9.1.

Tracks and Photons Efficiencies	
Track Efficiency	9.7
SinglePhoton Efficiency	5.7
Total Systematic Error	11.3

Table 9.1: Systematic errors in % due to tracking and single-photon efficiencies in this analysis.

9.2.2 K_L^0 Energy and Efficiency

Only a small fraction of the K_L^0 energy is deposited in the electromagnetic calorimeter. The not detected energy and momentum from the K_L^0 adds to E_{miss} and p_{miss} which is used to reconstruct the neutrino.

Energy Correction: The reconstructed K_L^0 energy in the simulation deviates from the reconstructed energy in data and hence one corrects that by scaling the energy. To estimate the systematic error the scale factors are varied within their uncertainties given by *BABAR* analysis document 1191 [24]. The resulting systematic error is given in Table 9.2.

Efficiency: As performed for tracks and photons a systematic error on the K_L^0 reconstruction efficiency is considered: clusters which are matched to a true K_L^0 are eliminated with a certain probability [24]. The killing probability is varied within its uncertainty to estimate the systematic error. The resulting systematic error is listed in Table 9.2.

Systematic errors for K_L^0 Energy and Efficiency	
K_L^0 Energy Smearing	2.8
K_L^0 Efficiency	1.4
Total Systematic Error	3.1

Table 9.2: Systematic error in % for energy smearing and efficiency for $B^+ \to \eta(\to \gamma\gamma)\ell^+\nu$.

9.2.3 Lepton Identification

The uncertainty for electron and muon identification are taken from other *BABAR* analyses. They quote a systematic error of 1.4% [26] and 3.0% [27] for electrons and muons respectively. For this analysis this results in an average value of 1.7%.

9.2.4 $\eta \to \gamma\gamma$ Reconstruction Efficiency

A study of $\pi^0 \to \gamma\gamma$ efficiency is described in *BABAR* analysis document 870 [25] which states a systematic error of 3.0%. The authors recommendation is to use the systematic error of the π^0 study for this $\eta \to \gamma\gamma$ analysis.

9.3 Physics Modeling

9.3.1 Signal Form Factor

For the systematic error on the signal form factor an assessment of the effect of the form factor model used is necessary. This uncertainty has not been evaluated yet and a value from a $B \to \pi\ell\nu$ analysis [29] is used, which is 2.2%.

9.3.2 Uncertainties in the $B \to X_u\ell\nu$ Modeling

Form Factor: The systematic error on the form factors has not been evaluated yet.

Branching Fraction: The branching fractions of the various Monte Carlo sources have an uncertainty and the branching fractions are varied within their uncertainty. The resulting errors are summarized in Table 9.3.

9.3.3 Uncertainties in the $B \to X_c\ell\nu$ Modeling

The systematic error calculation for $B \to X_c\ell\nu$ uncertainties consist of two contributions: the systematic error on the branching fractions and on the form factor.

Systematic errors for $B \rightarrow X_u \ell \nu$ modeling	
Decay	Error in %
$B^+ \rightarrow \eta$ FF	2.2
$B \rightarrow X_u \ell \nu$ FF	to be determined
$\mathcal{B}(B \rightarrow \pi \ell \nu)$	1.7
$\mathcal{B}(B \rightarrow \rho \ell \nu)$	5.0
$\mathcal{B}(B^+ \rightarrow \omega \ell^+ \nu)$	2.1
$\mathcal{B}(B^+ \rightarrow \eta' \ell^+ \nu)$	2.1
non-resonant $\mathcal{B}(B \rightarrow X_u \ell \nu)$	8.6
Total sys.error due to BF's	10.5

Table 9.3: Systematic errors in % due to $B \rightarrow X_u \ell \nu$ modeling.

Form Factor Parameters: Vector mesons have three form factor parameters. In the decay $B \rightarrow D^* \ell \nu$ these are $R1$, $R2$ and ρ^2 and they are varied within $\pm 1\sigma$. The existing correlations between the parameters are neglected and hence variations are done independently.

Branching Fraction: For the uncertainty on the branching fraction the branching fractions of $B \rightarrow D\ell\nu$, $B \rightarrow D^\star \ell\nu$, and $B \rightarrow D^{\star\star}\ell\nu$ is varied one by one within their error ranges

The systematic errors for the form factors and the branching fractions for the $B \rightarrow X_c \ell \nu$ modeling are given in Table 9.4.

Systematic errors for $B \rightarrow X_c \ell \nu$ modeling	
Decay	Error in %
Form Factor	2.1
Branching Fraction	4.1

Table 9.4: Systematic errors in % due to $B \rightarrow X_c \ell \nu$ modeling.

9.3.4   Continuum Uncertainties

An uncertainty on the normalization of the continuum background is assigned because it is fixed in the fit and not fitted. Assuming a 20% uncertainty on the normalization (see Table 6.5 in Chapter 6) the analysis is repeated with continuum scaled up by 20% and scaled down by 20%. The error in the Table 9.5 gives the resulting systematic error.

Systematic error for continuum	
Normalization	15.2

Table 9.5: Systematic errors in % on the normalization of the continuum background.

Studies of f_{Xclnu}							
	nominal	cont up	cont up	$B \to X_u \ell \nu$ up	$B \to X_u \ell \nu$ down	track	cluster
f_{Xclnu}	1.10	1.06	1.13	1.07	1.12	1.11	1.12

Table 9.6: Studies of f_{Xclnu} for the different systematic error calculation.

9.4 Other Systematic Uncertainty

9.4.1 Number of B Mesons Produced

The uncertainty on the number of B mesons produced directly translates into the uncertainty on the measurement of the branching fractions which is known to 1.1% [28]. An uncertainty of 1.1% for this systematic error is used.

9.5 Study for f_{Xclnu}

A study of the origin of the large deviation of f_{Xclnu} from 1.0 was performed. The results are shown in Table 9.6. It was found that the the scaled continuum (20% up and 20% down) has an effect about 4.5% on the fit factor f_{Xclnu}. The uncertainty on the $B \to X_u \ell \nu$ has an effect of 3.6% and the reconstruction uncertainties influances f_{Xclnu} in the 1% range. This can not explain the high deviation of the fit factor but may be a part of the discrepancies.

9.6 Summary of Systematic Uncertainties

All systematic error included in this analysis are summarized in Table 9.7. The systematic errors on the form factors of the signal and the $B \to X_u \ell \nu$ background have not been evaluated yet and are not included. The biggest systematic errors are the errors for the $B \to X_u \ell \nu$ form factor and the track and photons efficiencies as well as the error on the continuum. All other systematic errors are below 4.1%.

Summary of systematic errors in %	
Track Efficiencies	9.7
Photon Efficiencies	5.7
K_L Energy Correction	2.8
K_L Efficiency	1.4
Lepton Identification	1.7
$\eta \to \gamma\gamma$ Identification	3.0
Signal Form Factor	2.2
$B \to X_u \ell \nu$ FF	-
$B \to X_u \ell \nu$ BF	10.5
$B \to X_c \ell \nu$ FF	2.1
$B \to X_c \ell \nu$ BF	4.1
Continuum	15.2
$N_{B\bar{B}}$	1.1
Total	22.7

Table 9.7: Summary of systematic errors in %.

Chapter 10

Discussion

10.1 Discussion of the Results

A measurement of the branching fraction of the exclusive charmless semileptonic decay $B^+ \to \eta \ell^+ \nu$ with $\eta \to \gamma\gamma$ is presented. This is the first time this decay is studied as an untagged analysis in the *BABAR* experiment. The advantage of an untagged analysis versus a tagged analysis is the much higher signal efficiency, the disadvantage is a lower purity of the data sample. Currently the untagged analysis is expected to give the best results since the data statistic is still low.

In this analysis the signal and the largest background sample $B \to X_c \ell \nu$ are simultaneously fitted in the m_{ES} versus ΔE distribution (Chapter 7). By also fitting the $B \to X_c \ell \nu$ background, the systematic uncertainty due to the dominant background source is reduced.

In Chapter 8 stability tests are performed. The fit to the electron and muon sample results in discrepancies which are yet not understood. Problems are also seen if one relaxes the missing mass cut: the signal yield decreases. Further studies need to be performed to understand these discrepancies.

The branching fraction of $B^+ \to \eta \ell^+ \nu$ with $\eta \to \gamma\gamma$ is measured. The analysis used an integrated on-peak luminosity of 215 fb^{-1}, which corresponds to 225 million $B\bar{B}$ events and yielded 98.7 ± 27.1 $B^+ \to \eta(\to \gamma\gamma)\ell^+\nu$ events. The relative statistical uncertainty is 27% and the systematic error is 23%:

$$\mathcal{B}(B^+ \to \eta(\to \gamma\gamma)\ell^+\nu) = (1.28 \pm 0.35 \pm 0.29) \cdot 10^{-5} \qquad (10.1)$$

where the first error is the statistical error from the fit and the second error refers to the systematic uncertainties. It should be noted that the given systematic error calculation is not complete, for instance a proper evaluation of the uncertainties due to the signal form factor or the form factor uncertainties of the $B \to X_u \ell \nu$ background is still missing.

Using the $\eta \to \gamma\gamma$ branching fraction $\mathcal{B}(\eta \to \gamma\gamma) = 39.38 \pm 0.26\%$ [15] and Equation 10.1 one can quote a branching fraction of $B^+ \to \eta \ell^+ \nu$:

$$\mathcal{B}(B^+ \to \eta \ell^+ \nu) = (3.25 \pm 0.89 \pm 0.74 \pm 0.02) \cdot 10^{-5} \qquad (10.2)$$

where the first error is the statistical error from the fit, the second error refers to the systematic uncertainties, and the third error is due to the uncertainty on the PDG value for the $\eta \to \gamma\gamma$ branching fraction.

As mentioned in the introduction two measurements of this decay mode already exist. The CLEO collaboration presented an untagged measurement in 2003 using 9.7 million $B\bar{B}$ events which resulted in about 15 $B^+ \to \eta\ell^+\nu$ decays [3]. The measured branching fraction was $\mathcal{B}(B^+ \to \eta\ell^+\nu) = (8.4 \pm 3.1 \pm 1.6 \pm 0.9) \cdot 10^{-5}$, where the errors are statistical, systematic, and due to form-factor uncertainties. CLEO has recently updated this analysis (December 2006) and there are preliminary results for the branching fraction available: $\mathcal{B}(B^+ \to \eta\ell^+\nu) = (4.4 \pm 2.3 \pm 1.1 \pm 0.0) \cdot 10^{-5}$ [30].

In 2006 the *BABAR* collaboration presented a measurement [4] which was a tagged analysis with the *BABAR* experiment using a much larger data sample corresponding to an integrated luminosity of 316 fb^{-1}, which yielded 45.9 ± 7.1 $B^+ \to \eta\ell^+\nu$ decays. This measurement yielded a branching fraction of $\mathcal{B}(B^+ \to \eta\ell^+\nu) = (8.4 \pm 2.7 \pm 2.1) \cdot 10^{-5}$, where the first error is statistical and the second systematic.

The branching fraction measurement presented in this analysis is 1.3σ lower than the older CLEO measurement and 1.4σ lower than the result from the *BABAR* analysis. The preliminary results from the CLEO analysis is consistent only 0.4σ away from this analysis. The presented measurement of the branching fraction is the statistical most precise measurement so far. The systematic uncertainties evaluated so far are of comparable size.

10.2 Outlook

The changes made to the analysis framework to incorporate the $B^+ \to \eta(\to \gamma\gamma)\ell^+\nu$ decay in the already existing analysis framework for studies of $B \to \pi\ell\nu$ and $B \to \rho\ell\nu$ were made in a general way. Thus allowing studies of decays of semileptonic decays where the signal decay produces a hadronic final state with three or more particles.

To further improve and extent the analysis of the $B^+ \to \eta\ell^+\nu$ decay one could do one of the following possibilities:

- including a larger data sample,

- including more of the decay modes of the η meson e.g. $\eta \to \pi^+\pi^-\pi^0$ or $\eta \to \pi^0\pi^0\pi^0$,

- including more background samples in the fit to reduce the systematic uncertainties due to the background modeling,

- a q^2 dependent measurement of the branching fraction to study the q^2 dependence of the $B \to \eta$ form factor, and

- extraction of a value for $|V_{ub}|$,

Using the knowledge about the $B^+ \to \eta \ell^+ \nu$ decay one can also start to study the decay of $B^+ \to \eta' \ell^+ \nu$, where only upper limits have been reported [4]. Some of these possible steps have been studied in the recent months but are not ready for this diploma thesis.

Bibliography

[1] Heavy Flavor Averaging Group, http://www.slac.stanford.edu/xorg/hfag/.

[2] J. Dingfelder, Study of Charmless Semileptonic Decays $B \to \pi\ell\nu$ and $B \to \rho\ell\nu$ with Neutrino Reconstruction, *BABAR* Analysis Document 1520 (2007).

[3] S.B. Athar, et al. Study of the q^2-Dependence of $B \to \pi\ell\nu$ and $B \to \rho(\omega)\ell\nu$ Decay and Extraction of $|V_u b|$, CLEO Collaboration, [hep-ex/0304019], (2003).

[4] A. D'Orazio, Measurement of Branching Fractions of Exclusive Charmless Semileptonic Decays using the Recoil of Fully Reconstructed B mesons,*BABAR* Analysis Document 1537 (2006).

[5] P. Ball and R. Zwicky, Improved analysis of $B \to \pi\ell\nu$ from QCD sum rules on the light-cone, JHEP **10**, 019 (2001).

[6] D. Scora, N. Isgur, Semileptonic meson decays in the quark model: An update, Phys. Rev. **D52**, 2783-2812 (1995).

[7] P. Ball,Z. Zwicky, Improved analysis of $B \to \pi\ell\nu$ from QCD sum rules on the light-cone, JHP **10**, 019 (2001).

[8] P. Ball,Z. Zwicky, Phys. Rev.Phys. Rev. **D71**, 014015 (2005), e-Print Archive: hep-ph/0406232.

[9] P. Ball,Z. Zwicky, Phys. Rev.Phys. Rev. **D71**, 014029 (2005), e-Print Archive: hep-ph/0412079.

[10] M. Okamoto, et al., Semileptonic $D \to \pi/K$ and $B \to \pi/K$ decays in a $2 + 1$ flavor lattice QCD, e-Print Achive: hep-lat/04080116.

[11] F. De Fazio and M. Neubert, $B \to X_u\ell\nu$ decay distributions to order α_s, JHEP **06**, 017 (1999).

[12] B. Aubert, et al, The *BABAR* Detector, Nuclear Instruments and Methods in Physical Research A 479, (2002).

[13] *BABAR* Collaboration, The DIRC Particle identification System of the *BABAR* Experiment, SLAC Pub 10516, (2004).

[14] S. Spanier, et al., Kaon Selection at *BABAR*, *BABAR* Analysis Document 116, (2002).

[15] W.-M. Yao et al., Journal of Physics G 33, 1, (PDG)(2006).

[16] D. Fortin, http://www.slac.stanford.edu/bfroot/www/physics/analysis/awg/ - inclusivesl/common/dominiquehybrid.html/hybrid.html, (2004), Internal *BABAR* webpage.

[17] T. Sjostrand, The PYTHIA and JETSET programs, Prepared for Particles and Fields 92: 7th Meeting of the Division of Particles Fields of the APS (DPF 92), Batavia, Illinois, 10-14 Nov 1992.

[18] A.J. Weinstein, Study of Exclusive Charmless Semileptonic Decays of the B Meson, PhD Thesis, Stanford University (2004).

[19] W.A. Walkowiak, Pdf for CP violation and mixing including mistags due to partial reconstruction, *BABAR* Analysis Document 391 (2003).

[20] A. Mohapatra, Studies of A Neural Net Based Muon Selector for the BaBar Experiment, *BABAR* Analysis Document 474 (2004).

[21] http://www.slac.stanford.edu/BFROOT/www/doc/workbook/eventinfo/ BtaCandInfo/RunLists/PhotonLists.html, Internal *BABAR* webpage.

[22] S. Brunet Exclusive semileptonic $b \to u$ skim, *BABAR* Analysis Document 740 (2005).

[23] R. J. Barlow and C. Beeston, Fitting using Finite Monte Carlo Samples, Comput. Phys. Commun. **77**, 219–228 (1993).

[24] M. Pelliccioni, A study of KL identification and efficiencies, *BABAR* Analysis Document 1191 (2006).

[25] M.T. Allen, et al, A Study of Pi-zero Efficiency, *BABAR* Analysis Document 870 (2004).

[26] B. Aubert et al., BABAR Collaboration, Measurement of the ratio $\mathcal{B}(B^+ \to X\ell\nu)/\mathcal{B}(B^0 \to X\ell\nu)$, accepted for publication in Physical Review D, hep-ex/0607111.

[27] B. Aubert et al., BABAR Collaboration, Measurement of the CKM matrix element $|V_{ub}|$ with charmless exclusive semileptonic B meson decays at *BABAR*(2002). SLAC-PUB-9618, BABAR-PUB-02-15, Phys.Rev.Lett.90:181801,2003; e-Print Archive: hep-ex/0301001.

[28] C. Hearty, Hadronic Event Selection and B-Couning for Inclusive Charmonium Measurements, *BABAR* Analysis Document 30 (2000).

[29] A.J. Weinstein, Study of Exclusive Charmless Semileptonic Decays of the B Meson, *BABAR* Analysis Document 531 (2005).

[30] Preliminary results by the CLEO Collaboration, presented by Sheldon Stone at the CKM 2006 Workshop, Nagoya, Japan; see parallel session agenda at http://agenda.hepl.phys.nagoya-u.ac.jp/conferenceDisplay.py?confId=2#4".

List of Figures

List of Tables

Erklärung

Ich versichere, dass ich diese Arbeit selbständig verfaßt und keine anderen als die angegebenen Quellen und Hilfsmittel benutzt habe.

Heidelberg, den 15. Februar 2007   _____